Numerical analysis of effects of fins and conductive walls on heat transfer in side heated cavities — Onset of three-Dimensional phenomena in natural convection

Vesper, J. Elin; Tietjen, Sebastian C.; Chakkingal, Manu; Kenjereš, Saša

DOI
10.1016/j.ijheatmasstransfer.2021.122033

Publication date
2022

Document Version
Final published version

Published in
International Journal of Heat and Mass Transfer

International Journal of Heat and Mass Transfer 183 (2022) 122033

Contents lists available at ScienceDirect

International Journal of Heat and Mass Transfer

journal homepage: www.elsevier.com/locate/hmt

Numerical analysis of effects of fins and conductive walls on heat transfer in side heated cavities — Onset of three-dimensional phenomena in natural convection

J. Elin Vesper[a,b,*], Sebastian C. Tietjen[a], Manu Chakkingal[a,b], Saša Kenjereš[a,b]

[a] Transport Phenomena Section, Department of Chemical Engineering, Faculty of Applied Sciences, Delft University of Technology, Van der Maasweg 9, 2629HZ Delft, The Netherlands
[b] J.M. Burgerscentrum for Fluid Mechanics, Mekelweg 2, 2628 CD Delft, The Netherlands

ARTICLE INFO

Article history:
Received 25 February 2021
Revised 23 September 2021
Accepted 27 September 2021
Available online 23 November 2021

Keywords:
Natural convection
Side heated cavity
Differentially heated cavity
Finned cavity
Conductive walls
Heat transfer
Stratification
Instabilities

ABSTRACT

In the present study, we analyse individual and combined effects of conductive horizontal walls and conductive fins on the natural convection of air in side heated cavities (SHC). The flow and heat transfer are studied for Rayleigh numbers in the range of $10^4 - 10^9$: Direct Numerical Simulation (DNS) is conducted for the lower and Large Eddy Simulation (LES) for the higher Rayleigh numbers ($> 10^8$). Thermally conductive walls destabilize the flow yielding an earlier transition to turbulence and expedite the decay in boundary layer thickness with increase in Rayleigh number. The preheating/precooling along the conductive walls reduces the actual heat transfer at the vertical walls. Above the fin, instabilities are only marginally enhanced for adiabatic horizontal walls, whereas for conductive horizontal walls, plumes erupt from the fin. This localized Rayleigh-Bénard-like effect triggers 3D instabilities in the entire flow field and yields a steeper slope in Nusselt-Rayleigh diagram. The presence of a fin increases the integral heat transfer by 18% for adiabatic and 21% for conductive horizontal walls. We show that 2D and 3D simulations are similar for the smooth cases (i.e., without fin), but differ by 4% and 13% for the adiabatic and conductive fin cases respectively. The local heat transfer characteristics even deviates up to 50%, therefore a 2D simplification should be avoided.

1. Introduction

Natural convection in side heated cavities (SHC) represents the heat transfer in several setups in daily life and industry. For example, the SHC model applies to traditional double-glazed windows, which are installed to provide a better thermal insulation of buildings [1]. Another example is a static refrigerator, in which the condenser can be considered as the cold wall and the door of the refrigerator as the hot wall [2]. Further examples can be found in low-heat-flux cooling of electronic devices [3], drying vegetables in food industry [4,5], and passive air conditioning of residential and office space [6]. (Another important setup of natural convection in internal flows is the Rayleigh-Bénard convection, in which the setup is rotated by 90° with the hot wall at the bottom and the cold wall at the top producing thermal plumes. The most general case of inclining a cavity and thus modelling the range from RBC to a SHC flow was studied by Williamson et al. [7]. While both have applications and the description of their heat transfer is not trivial, we focus in the following on the SHCs.) Besides natural convection, radiation may play a crucial role in heat transfer in such systems, which may not only add to the convective heat transfer, but also change the flow characteristics [8,9]. If the temperature difference is small the heat transfer due to radiation is considerably smaller than the one due to convection [3], latter being the case in the current study and hence the effect of radiation is not considered.

The relevance of heat transfer in SHCs in these various technological fields has initiated numerous theoretical, experimental, and numerical studies. In 1954, Batchelor [10] pioneered the research on SHCs with an elaborate theoretical analysis of heat transfer. His work was driven by the practical application of insulating houses and focused on the 2D laminar case with adiabatic horizontal walls. He briefly mentioned a possible transition to turbulence for strong convection. Elder [11] identified experimentally the laminar, the transitional, and the developed turbulent regimes in a SHC depending on the Rayleigh number. Several studies [12,13] were dedicated to identify the transition between the laminar and turbu-

* Corresponding author.
E-mail address: j.e.vesper@tudelft.nl (J.E. Vesper).

https://doi.org/10.1016/j.ijheatmasstransfer.2021.122033

Nomenclature

Abbreviations

DEDM	Dynamic eddy diffusivity model
DNS	Direct numerical simulation
FC-CHW	Finned cavity with conductive horizontal walls
FC-AHW	Finned cavity with adiabatic horizontal walls
LES	Large eddy simulation
LSC	Large scale circulation
RBC	Rayleigh-Bénard-Convection
SC-AHW	Smooth cavity with adiabatic horizontal walls
SC-CHW	Smooth cavity with conductive horizontal walls
SHC	Side heated cavity
WALE	Wall-adapting local eddy-viscosity

Dimensionless numbers

Nu	Nusselt number
Pr	Prandtl number
Ra	Rayleigh number
Re	Reynolds number

Greek Symbols

α	Thermal diffusivity, m^2/s
β	Coefficient of volume expansion of fluid, K^{-1}
δ_u	Normalised viscous boundary layer thickness
δ_{th}	Normalised thermal boundary layer thickness
ν	Kinetic viscosity, m^2/s
ρ	Density, kg/m^3
Θ	Normalised temperature

Roman Symbols

$A = \frac{H}{L}$	Cavity aspect ratio
g	Gravity, m/s^2
H	Cavity height, m
h	Heat transfer coefficient, $W/(m^2K)$
k	Thermal conductivity, $W/(mK)$
L	Cavity width, m
p	Pressure, $kg/(ms^2)$
T	Temperature, K
t	Time, s
u	Velocity, m/s
x, y, z	represent the cartesian coordinates

Superscripts

$\widehat{\ }$	LES filter
$\widetilde{\ }$	LES test filter

Subscripts

C	Cold
f	Fin
H	Hot
n	Normal to the wall
sgs	Subgrid scale
w	Wall

lent regime for SHCs. Trias et al. [14,15] numerically investigated the changes in velocity field with the onset of turbulence. They observed that the transition point, at which the laminar boundary layer at the vertical walls transits to a turbulent one, shifts further upstream with increasing Rayleigh number. This results in a smaller stratified core region. The onset of turbulence is of such particular interest, as the mixing induced by coherent flow structures (eddies) may enhance heat transfer.

In the literature, the heat transfer efficiency is quantified in terms of the Rayleigh-Nusselt relation. Yu et al. [16] identified the laminar Rayleigh-Nusselt power-law-scaling $Nu \sim Ra^{0.31}$ for the range $Ra = 10^3$–10^7, using 2D simulations to exclude any influence of three-dimensional instabilities. They argued that if the heat transfer outside the boundary layer is dominated by convection and the boundary layer is sufficiently thin, the scaling should be comparable to the one for the well-studied Rayleigh-Bénard convection, for which the Rayleigh-Nusselt power-law-scaling coefficient approaches 1/4 for the laminar regime and 1/3 for the turbulent regime [17]. For SHCs, Lankhorst [18] showed that the local Nusselt number scales with 1/4 for the first section of the vertical walls, where the flow is laminar, while it switches to 1/3 further downstream, when turbulence sets in. This defines the scope for scaling in natural convection rather broadly, which leaves much space for improvement in heat transfer through changes, which trigger an earlier transition to turbulence, e.g., geometry modifications or unstable thermal layering.

Concurrent to the advances in research on the classical SHC setup introduced by Batchelor, interest rose to adapt the SHC model closer to reality: (i) Conductive horizontal walls were added to better represent cavities made out of highly conductive materials such as metal and (ii) fins were attached to the side walls, as they are often used in industrial and technological applications to enhance heat transfer, (iii) turbulence models were introduced to achieve simulations at higher Rayleigh numbers and (iv) 3D setups with periodic boundary conditions replaced 2D setups to capture the effect of 3D turbulent structures. Next, we will shortly outline these developments, partially in their entangled form, as these steps were often undertaken simultaneously.

1.1. Conductive horizontal walls

Lankhorst [18] studied the natural convection in a 2D SHC for both adiabatic and fully conductive horizontal walls (i.e., the temperature varies linearly from the cold to the hot wall). He showed that the transition between the laminar and the turbulent regime begins earlier for conductive horizontal walls due to an unstable stratification. The fluid precools (or preheats) in the boundary layer at the conductive horizontal walls before arriving at the vertical walls. Consequently, the heat transfer at the vertical walls reduces due to a lower temperature difference between the impinging fluid and the wall. In the turbulent regime, the eddy viscosity is up to three times higher along the vertical walls, and hence the core is less stratified in comparison to cavities with adiabatic horizontal walls. Fusegi et al. [19] confirmed the enhancement of velocity fluctuations when using conductive horizontal walls. Henkes and Le Quéré [20] determined the transition point for adiabatic and conductive horizontal walls in 2D and 3D simulations in terms of Rayleigh number. The onset of turbulence occurred at a lower Rayleigh number for fully conductive walls.

With increasing computational power, Sebilleau et al. [21] were the first to numerically analyze cavities with horizontal conductive walls for the 3D case at high Rayleigh numbers. They simulated both the weakly and the fully turbulent regime ($Ra = 10^8$–10^{11}). They have shown that the stratification decreased for higher Rayleigh numbers, which is in agreement with previous research such as Lankhorst's [18] study in the laminar regime. Their obtained Rayleigh-Nusselt scaling of $Nu \sim Ra^{0.32}$ is similar to the one for adiabatic horizontal walls. Sergent et al. [22] investigated realistic cavities with horizontal boundary conditions based on experimental data. These boundary conditions can be considered as a blending of adiabatic and fully conductive walls.

1.2. Fins

Rarely the geometries are perfect empty cavities but come along with obstacles of various sizes and shapes [23,24]. They are either system necessities such as electronic devices, which act

as heat sources [23,25] or are specifically added to enhance heat transfer. In the latter case, especially fins are applied [26,27], as these small modifications impact the flow without the need to change the outer geometry. Fins can be attached to the heated wall to increase the heat transfer in a passive safety system for nuclear power plants [28]. Fins are also added to thermal solar collectors and heat exchangers to improve the heat transfer efficiency [29,30]. Considering its frequent use in industry, several numerical studies have been carried out on a fin attached to a side wall. The fin was either fully conductive (i.e., it has the same temperature as the wall it is attached to) [27,31], or adiabatic [32–34]. While studies find different conclusions on whether adiabatic fins increase or decrease the heat transfer [27,35], the literature agrees that fully conductive fins increase the global heat transfer [26,27]. The heat transfer can be further increased by optimizing the fin length and thickness [26,27]. The optimal location of the fin attached to the side-wall was observed to be approximately at its mid-height [27,36]. Fins too close to the top prevent flow above the fin, so that the fin can only transfer heat to the flow at its lower side. Fins attached too close to the bottom, reduce the global heat transfer since the fin creates a zone of hot fluid at the bottom, in which the temperature gradient disappears [31]. A conductive fin at the hot wall evokes an intrusion zone of hot fluid underneath the fin, and the flow oscillates above the fin for higher Rayleigh numbers [32]. The oscillating behavior causes instabilities in the boundary layers, which may trigger turbulence earlier in comparison to a smooth (non-finned) case.

1.3. Turbulence modeling

As it is tedious to conduct experiments over a wider range of Rayleigh numbers and resolved direct numerical simulations (DNS) are at present still limited to relatively low Rayleigh numbers, turbulence models need to be introduced to reach high Rayleigh number regimes. Computationally less expensive Reynolds-Averaged Navier-Stokes (RANS) Simulations of SHCs were reported in literature [18,37]. Large Eddy Simulation (LES) models resolve important flow and thermal structures providing a more detailed picture than RANS. Peng and Davidson [38] performed LES in the weakly turbulent regime ($Ra = 1.58 \times 10^9$) for a SHC. They used a Dynamic Smagorinksy Model for calculating the subgrid eddy viscosity and calculated the subgrid thermal diffusivity via the turbulent Prandtl number. The authors concluded that their simulations are in reasonable agreement with the experiments of Tian [39]. Barhaghi and Davidson [40] showed that both the dynamic Smagorinksy model and the wall-adapting local eddy-viscosity (WALE) model can predict the transition point correctly, but the Nusselt number is marginally under-predicted and turbulent flow structures are over-predicted. Pilkington and Rosic [41] compared the Dynamic Smagorinsky, WALE, and Dynamic Kinetic Energy subgrid model for an air-filled cavity and concluded that all of them predict the total heat flux reasonably well, but over-predict the temperature fluctuations. It can be concluded that state-of-the-art LES captures natural convection better than RANS, but additional research is still needed to find an optimal LES subgrid closure.

1.4. Two-Dimensional versus three-Dimensional simulations

Due to the high computational cost involved in three-dimensional simulations, many earlier natural convection studies are constrained to two dimensions [42–44], which may come at the expense of accurately representing three-dimensional effects, which are often important in natural convection. Henkes and Le Quéré [20] showed that for 3D simulations the transition to turbulence occurs at a lower Rayleigh number compared to the 2D case. Due to the computation power limitations, they used only a depth of $0.1L$ for the 3D simulation, which is not sufficient to resolve all 3D structures. Toru et al. [45] found a significant discrepancy in Nusselt number between the 2D and 3D simulations due to the additional velocity fluctuations in the quasi-homogeneous direction, which they found to be one order of magnitude smaller than the other two components and increasing in strength with higher Rayleigh numbers.

Lankhorst [18] observed a similar increase in velocity in the third dimension for conductive horizontal walls. He also investigated conductive horizontal boundary conditions in the laminar regime ($Ra = 10^6 - 10^8$) and determined one order of magnitude higher velocities than for adiabatic horizontal walls. Moreover, he observed that 2D simulations underpredict the heat transfer for SHCs with conductive horizontal walls.

For the transition and turbulent regime (which occurs in the range $Ra = 6.4 \times 10^8 - 1 \times 10^{10}$), Trias et al. [46,47] found a significant impact of 3D-effects on turbulent second-order statistics and the local Nusselt number. They identified that the oscillations were significantly more robust in 2D, and the large eddies were rapidly dissipated for 3D simulations. The fast dissipation increased with higher Rayleigh number and reduced the overall large-scale mixing effect. Recently, Miroshnichenko and Sheremet have summarized the research on natural convection in cavities and have found that despite a growing computational power only few three-dimensional studies were conducted [48].

1.5. Aim of the present study

In spite of its relevance in industrial applications, the combination of horizontal conductive walls and conductive fins has not been studied so far, to the best of the authors' knowledge. In the present paper, we address the effect of substituting the horizontal walls with conductive ones and attaching a fully conductive fin to the hot wall. We investigate the heat transfer in the Rayleigh range of $Ra = 10^4 - 10^9$, where we use DNS for the full range of the 2D case as well as for $Ra = 10^4 - 10^7$ for the 3D case. For $Ra = 10^8 - 10^9$, we use LES for the 3D simulations. We also aim at determining, how the previously mentioned features effect the 3D structures and how well the 2D studies represent the flow physics.

The paper is organised as follows: In Section 2, we introduce the four case setups investigated in the current study, followed by the discussion of the numerical method in Section 3. In Section 5, first we analyze the velocity and temperature field to show the interplay between convection and driving buoyancy force. Then we use the Q-criterion to visualize vortices. These affect the boundary layer thicknesses shown afterwards, which in turn determine local and integral heat transfer, from which the latter is depicted in Nusselt-Rayleigh diagrams. The section ends with a comparison of selected 2D and 3D simulations to sketch under which circumstances a reduction to two-dimensions is reasonable and when considering the third dimension is crucial. Section 6 states our conclusions.

2. Case setup

The natural convection is studied in a side heated cavity with a square cross section of dimensionless length L. The left wall is kept at a high temperature $T(x = 0, y, z) = T_H$, the right wall at a low temperature $T(x = L, y, z) = T_C$. We investigate the geometry either with smooth wall (i.e., without a fin) or one fully conductive fin. In the cases with a fin, the fin is attached to the left wall and is kept at the high temperature T_H.

For the horizontal walls, two different temperature boundary conditions were considered:

1. adiabatic walls — which are commonly chosen in literature [10,49], or

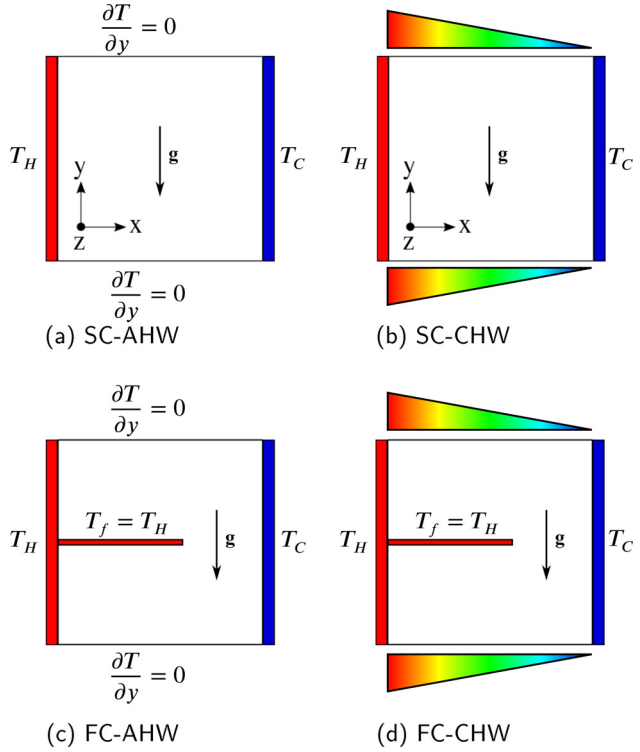

Fig. 1. 2D sketches of (a) a smooth cavity with adiabatic horizontal walls (SC-AHW), (b) a smooth cavity with conductive horizontal walls (SC-CHW), (c) a finned cavity with adiabatic horizontal walls (FC-AHW) and (d) a finned cavity with conductive horizontal walls (FC-CHW); periodic boundary conditions are applied in z-direction.

2. fully conductive walls (so that the temperature profile is varying linearly from the hot to the cold wall), which is more appropriate if the cavity walls are made of a highly conductive material such as metal (which exhibits a thermal conductivity three to four orders of magnitude higher than air under standard conditions),

$$T(x, y = 0, z) = T(x, y = H, z) = T_H - \left(\frac{T_H - T_c}{L}\right)x. \tag{1}$$

Fig. 1 shows the considered geometries with boundary conditions, which are (a) smooth cavity with adiabatic horizontal walls (SC-AHW), (b) smooth cavity with conductive horizontal walls (SC-CHW), (c) finned cavity with adiabatic horizontal walls (FC-AHW) and (d) finned cavity with conductive horizontal walls (FC-CHW). All walls (and the fin, if present) are no-slip boundaries with a zero-flux pressure boundary condition, ensuring that the buoyant forces acting on the wall are counter-balanced. In the quasi-homogeneous, spanwise z-direction periodic boundary conditions were applied. The spanwise width of the cavity was L for Rayleigh numbers up to 10^8. At higher Rayleigh numbers, the width was reduced up to a value, which still guarantees that it extends more than twice the biggest turbulent structure in a smooth cavity. To determine this value, we used the two-point correlation data for velocity and temperature presented by Sebilleau et al. [21]. The corresponding spanwise width W can be found in Table 2. To be consistent, the same depth is used for the finned cavity. The gravity g acts in negative y-direction. The fin is attached to the hot wall at half height extending $l/L = 0.6$ into the cavity and has a fin width $w/L = 0.02$. Elatar et al. [27] found that this height and length give an increased heat transfer for $Ra = 10^6$.

The entire problem is defined by two non-dimensional parameters, which are the Prandtl number and the Rayleigh number. For all the cases investigated, air was chosen as the working fluid with a Prandtl number of Pr=0.71. The Rayleigh number determines the thermal forcing and is given as

$$Ra = \frac{\beta \Delta T g L^3}{\nu \alpha}. \tag{2}$$

All four geometries were studied for Rayleigh numbers between $Ra = 10^4 - 10^9$.

Table 1
Considered cases and turbulence modeling approach.

Ra	Modeling	Case	Horizontal boundary conditions
$10^4 - 10^7$	DNS (2D/3D)	Smooth	Adiabatic
			Conductive
$10^4 - 10^7$	DNS (2D/3D)	Fin	Adiabatic
			Conductive
$10^8 - 10^9$	DNS (2D)	Smooth	Adiabatic
			Conductive
$10^8 - 10^9$	DNS (2D)	Fin	Adiabatic
			Conductive
$10^8 - 10^9$	LES (3D)	Smooth	Adiabatic
			Conductive
$10^8 - 10^9$	LES (3D)	Fin	Adiabatic
			Conductive

Table 1 summarizes the simulations carried out, both in 2D and 3D. DNS were carried in the range $Ra = 10^4 - 10^7$, and LES for $Ra = 10^8 - 10^9$ due to computational limitations. The meshing for DNS (Table 2) follows closely the analysis on natural convection by Shishkina et al. [50], who investigated the required numerical resolutions for Rayleigh-Bénard-Convection (RBC). Although the study is for RBC, it can be adapted for SHCs, since instabilities and thus small structures start to occur at a higher Rayleigh number than for RBC [21,37]. Table 2 summarizes the meshing parameters for the different cases.

Next to the overall mesh size, Shishkina et al. suggest a required number of cells in the *Boundary Layer* (BL). All domains are meshed with at least one cell more than needed for the BL (2) to accurately resolve all flow and thermal structures in the boundary layer. These requirements are also used for the 2D cases of $Ra = 10^8$ and $Ra = 10^9$. For LES, the DNS boundary layer requirements by Shishkina et al. [50] are maintained, since we perform wall-resolved LES. In the bulk region, the subgrid-scale model mimics the small scales and the cell size can be increased up to ten times the Kolmogorov scale. Thus, the number of cells decreases from 2.7 million at $Ra = 10^7$ to 1.2 million cells for same case at $Ra = 10^8$ when using LES for the example of the smooth case.

The mesh is chosen to be equidistant in spanwise direction for all Rayleigh numbers. From $Ra = 10^4 - 10^6$, the mesh was equidistant along all directions. For higher Rayleigh numbers, the cell size increases in a geometric progression of ratio $1.04 - 1.05$ with distance to the wall.

2.1. Mesh independence study

A mesh refinement study was conducted for the DNS simulation of the FC-CHW at $Ra = 10^7$ for three meshes of 1,1.6 and 2.7 million cells. Table 3 summarizes the meshing parameters. Fig. 2 depicts in (a) the time-averaged velocity in y-direction at $y = 0.6$ and in (b) the plane-averaged temperature as a function of x. The 1 M line overpredicts the mean velocity around the end of the fin tip. For the meshes with 1.6 M cells and 2.7 M cells both the mean y-velocity and plane-averaged temperature match. Thus, the mesh is already independent for 1.6 M cells. However, the simulation is carried out on the finest mesh (2.7 M cells), since we follow the high resolution requirements by Shishkina et al. [51].

Table 2
Meshing parameter for smooth and fin cases.

Simulation	Dimensions	Rayleigh	Smooth case		Fin case		Cells	*Requested*
Type	*LxHxW* [m]	number	Cells [*M*]	Cells *XxYxZ*	Cells [*M*]	Cells *XxYxZ*	in BL	*Cells in BL*
	$1 \times 1 \times 1$	10^4	0.6	$76 \times 100 \times 76$	0.5	$75 \times 98 \times 75$	14	*(1)*
	$1 \times 1 \times 1$	10^5	0.6	$76 \times 100 \times 76$	0.5	$75 \times 98 \times 75$	8	*(2)*
DNS	$1 \times 1 \times 1$	10^6	0.6	$76 \times 100 \times 76$	0.5	$75 \times 98 \times 75$	4	*(3)*
	$1 \times 1 \times 1$	10^7	2.7	$164 \times 164 \times 100$	2.7	$164 \times 164 \times 100$	6	*(4)*
	$1 \times 1 \times 1$	10^8	1.2	$110 \times 110 \times 110$	2.5	$166 \times 178 \times 83$	7	*(6)*
LES	$1 \times 1 \times 0.5$	10^9	1.8	$154 \times 154 \times 77$	3.3	$246 \times 256 \times 55$	9	*(8)*

Table 3
Meshing parameter for different mesh refinement levels for the DNS of the FC-CHW at $Ra = 10^7$.

Total number of cells	Cells *XxYxZ*
1 M	$100 \times 100 \times 100$
1.6 M	$128 \times 128 \times 100$
2.7 M	$164 \times 164 \times 100$

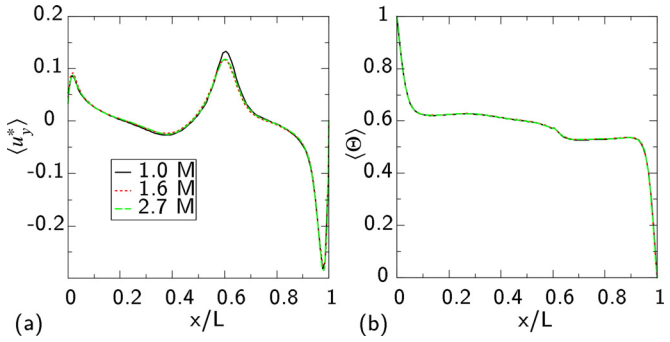

Fig. 2. For three different mesh refinements: (a) Mean velocity in y-direction along the line $y = 0.6$, (b) plane averaged temperature Θ over x for the conductive fin case at $Ra = 10^7$.

3. Governing equations and subgrid-Scale closure

At low Rayleigh numbers, the equations are resolved by DNS. Since the changes of transport properties and density are assumed to be small (i.e., $\beta \Delta T << 1$), constant molecular transport coefficients are used and density changes are only considered in the forcing of the momentum equation (which corresponds to the Boussinesq approximation). The incompressible Navier-Stokes equations then read as

$$\frac{\partial u_i}{\partial x_i} = 0\,, \tag{3}$$

$$\frac{\partial u_i}{\partial t} + \frac{\partial \left(u_i u_j\right)}{\partial x_j} = -\frac{1}{\rho_{ref}} \frac{\partial p}{\partial x_i} + \nu \frac{\partial^2 u_i}{\partial x_j \partial x_j} + \beta \left(\Theta - \Theta_{ref}\right) g_i\,, \tag{4}$$

$$\frac{\partial \Theta}{\partial t} + \frac{\partial \left(\Theta u_i\right)}{\partial x_i} = \alpha \frac{\partial^2 \Theta}{\partial x_i \partial x_i}\,, \tag{5}$$

where $\Theta = \frac{T - T_C}{T_W - T_C}$ is the dimensionless temperature and Einstein summation convention was applied.

A PISO solver [52] from the OpenFoam fork foam-extend 4.0 was used, namely *buoyantBoussinesqPisoFoam*. The details of the solver validation were reported by Chakkingal et al. [53]. A second-order backward temporal and a second-order central spatial discretization scheme were applied. A fixed time step size was chosen such that the Courant number was kept below 0.35.

For the cases at $Ra = 10^8 - 10^9$, we model the turbulence by wall-resolved Large Eddy Simulation (LES) using the wall-adapting local eddy-viscosity model (WALE) for the velocity and a dynamic model for the temperature field. The filtered transport equations read

$$\frac{\partial \hat{u}_i}{\partial x_i} = 0\,, \tag{6}$$

$$\frac{\partial \hat{u}_i}{\partial t} + \frac{\partial \left(\hat{u}_i \hat{u}_j\right)}{\partial x_j} = -\frac{1}{\rho_r} \frac{\partial \hat{p}}{\partial x_i} + \nu \frac{\partial^2 \hat{u}_i}{\partial x_j \partial x_j} - \frac{\partial \tau_{ij}^{sgs}}{\partial x_j} + \beta \left(\hat{\Theta} - \Theta_r\right) g_i\,, \tag{7}$$

$$\frac{\partial \widehat{\Theta}}{\partial t} + \frac{\partial \left(\widehat{\Theta} \hat{u}_i\right)}{\partial x_i} = \frac{\partial}{\partial x_i} \left(\alpha \frac{\partial \widehat{\Theta}}{\partial x_i} - J_i^{sgs} \right). \tag{8}$$

The deviatoric subgrid stress is closed by the eddy diffusivity assumption written as

$$\tau_{ij}^{sgs} - \frac{1}{3} \tau_{kk}^{sgs} \delta_{ij} = -2 \nu_{sgs} \widehat{S_{ij}} \tag{9}$$

$$\text{with} \qquad \widehat{S_{ij}} = \frac{1}{2} \left(\frac{\partial \hat{u}_i}{\partial x_j} + \frac{\partial \hat{u}_j}{\partial x_i} \right), \tag{10}$$

where the subgrid viscosity is modeled as $\nu_{sgs} = C_k \Delta \sqrt{k_{sgs}}$, and the subgrid kinetic energy is given by the WALE model as

$$k_{sgs} = \left(C_w^2 \frac{\Delta}{C_k} \right)^2 \frac{\left(\hat{S}_{ij}^d \hat{S}_{ij}^d \right)^3}{\left(\left(\hat{S}_{kl} \hat{S}_{kl} \right)^{\frac{5}{2}} + \left(\hat{S}_{kl}^d \hat{S}_{kl}^d \right)^{\frac{5}{4}} \right)^2},$$

with

$$\hat{S}_{ij}^d = \frac{1}{2} \left(\frac{\partial \hat{u}_i}{\partial x_k} \frac{\partial \hat{u}_k}{\partial x_j} + \frac{\partial \hat{u}_k}{\partial x_i} \frac{\partial \hat{u}_j}{\partial x_k} \right) - \frac{1}{3} \left(\frac{\partial \hat{u}_k}{\partial x_l} \frac{\partial \hat{u}_l}{\partial x_k} \right) \delta_{ij}\,,$$

where $C_k = 0.094$ and $C_w = 0.325$.

For the closure in the temperature equation, we assume the simple gradient diffusion hypothesis (SGDH) for the subgrid turbulent heat flux, which reads

$$J_i^{sgs} = -\alpha_{sgs} \frac{\partial \widehat{\Theta}}{\partial x_i}\,, \tag{11}$$

where the subgrid thermal diffusivity is expressed by the subgrid Prandtl number as $\alpha_{sgs} = \frac{\nu_{sgs}}{Pr_{sgs}}$. The subgrid Prandtl Pr_{sgs} number of the dynamic eddy diffusivity model (DEDM) using the dynamic procedure [54] is given by

$$\frac{1}{Pr_{sgs}} = \frac{1}{2 C_S} \frac{F_i H_i}{H_j H_j} = \frac{F_i H_i}{H_j H_j} \frac{M_{kl} M_{kl}}{M_{mn} L_{mn}}\,, \tag{12}$$

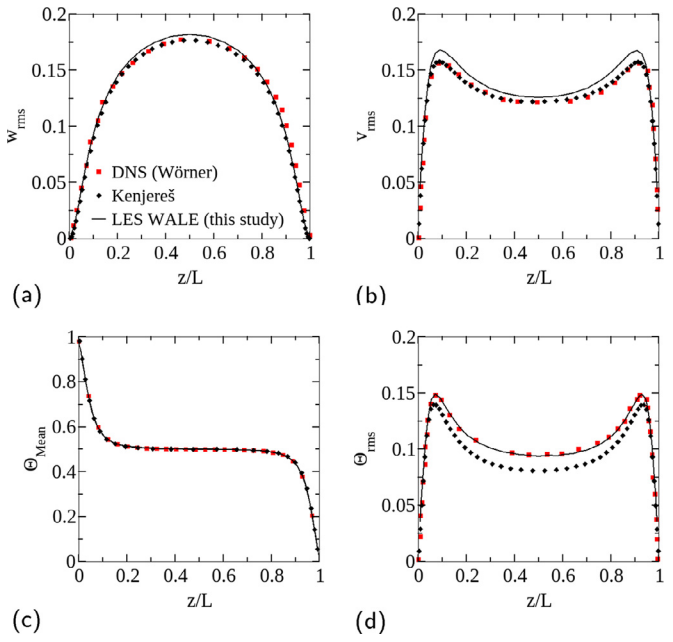

Fig. 3. Turbulent velocity and temperature statistics across the channel for Rayleigh-Bénard Convection for $Ra = 6.3 \times 10^5$. The normalization scales are $\Theta = \frac{T-T_c}{T_h-T_c}$ for the temperature, the plate distance L for the length and $\sqrt{g\beta\Delta TL}$ for the velocity. (a) Wall normal velocity fluctuations w_{rms}, (b) velocity fluctuations parallel to the wall v_{rms}, (c) mean temperature Θ_{mean} and (d) thermal fluctuations Θ_{rms}.

where the Leonard scalar flux $F_i = \widetilde{\widetilde{u_i}\widetilde{\Theta}} - \widetilde{\widetilde{u}_i}\widetilde{\widetilde{\Theta}}$ is the difference between the subgrid scalar flux at test filter scale and the one at filter scale. The modeled difference between the two scales is

$$H_i = \sqrt{2}\,\overline{\Delta^2 \left|\widehat{S}\right| \frac{\partial \widehat{\Theta}}{\partial x_i}} - \sqrt{2}\widetilde{\Delta}^2 \left|\widetilde{\widehat{S}}\right| \frac{\partial \widetilde{\widehat{\Theta}}}{\partial x_i}.$$

The second fraction in Eq. (12) is derived from the velocity field, where the corres ponding Leonard stress $L_{ij} = T_{ij} - \widetilde{\tau_{ij}^{sgs}}$ represents the stress contributions of scales between the filter scale and the test filter scale. The modeled stresses for the velocity are given by

$$M_{ij} = \sqrt{2.0}\Delta^2 \overline{\sqrt{\widehat{S_{kl}}\widehat{S_{kl}}}\widehat{S_{ij}}} - \sqrt{2.0}\widetilde{\Delta}^2 \sqrt{\widetilde{\widehat{S_{kl}}}\widetilde{\widehat{S_{kl}}}}\widetilde{\widehat{S_{ij}}}.$$

To stabilize the model, both the numerator and denominator are filtered, and the subgrid scale Prandtl number is clipped to values above zero.

3.1. Validation LES model

The WALE model is validated for turbulent Rayleigh-Bénard Convection at $Ra = 6.3 \times 10^5$. The Prandtl number is $Pr = 0.71$. The plates extend in both directions 6 times as far as the height between them, which gives a box of the dimensionless size $6 \times 6 \times 1$. The boundaries normal to the x- and y-direction are periodic. The grid refinement is $100 \times 100 \times 32$ with an equidistant spacing in x- an y-direction, a near-wall refinement ensuring $y_1^+ < 1$ and an average spacing of $< y^+ >= 0.29$ in z-direction.

Fig. 3 plots low-order turbulent statistics for the velocity and temperature over the channel height. The results are compared with DNS results by Wörner [55] and from an in-house code by Kenjereš [56,57]. The wall normal velocity fluctuations calculated by LES with a WALE model are in good agreement with the data by Wörner and from the in-house code. The spanwise velocity fluctuations are marginally overpredicted by the solver we used in the present study. Both the mean temperature and the thermal fluctuations are in an overall agreement with the DNS data. Differences between the results by Wörner and Kenjereš are probably caused by an insufficient sample size. For the latter, a sample-size independence study was conducted ensuring accurate statistics. Differences between the present dynamic LES and DNS in-house code can be accounted to the mesh resolution and modelling error.

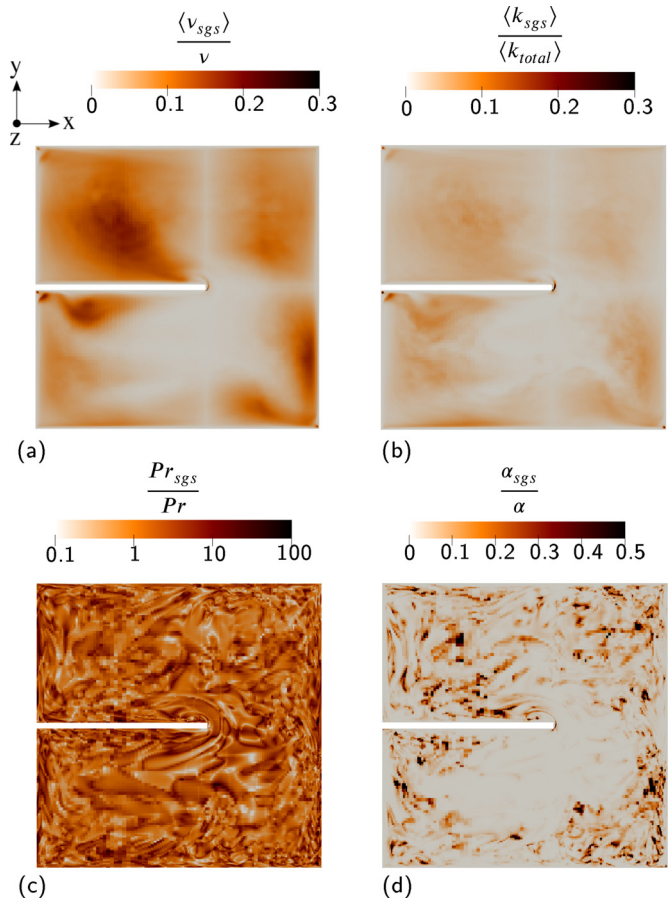

Fig. 4. LES resolution (a) mean subgrid-scale viscosity by molecular viscosity, (b) mean subgrid-scale kinetic energy divided by mean total turbulent energy, (c) subgrid-scale Prandtl number by molecular Prandtl number (note the logarithmic scaling), and (d) instantaneous subgrid-scale thermal diffusivity by molecular thermal diffusivity. The values are clipped to the range of the scales.

3.2. LES resolution

Fig. 4 shows the contribution of the subgrid-scale models for the FC-CHW at $Ra = 10^9$. The ratio between mean subgrid-scale viscosity and the molecular viscosity, shown in Fig. 4 (a), shows viscosity increments up to 0.2 due to the subgrid-scale viscosity in wall the neighborhoods and above the fin. The subgrid-scale kinetic energy contribution to the total turbulent kinetic energy (Fig. 4 (b)) is in most regions below 0.15, and thus below the postulated maximum for a well resolved LES by Pope [58]. The ratio between the instantaneous subgrid-scale and molecular Prandtl number fluctuates in the range $(2 \times 10^{-3}$–$3 \times 10^2)$ (Fig. 4 (c)). The instantaneous subgrid-scale thermal diffusivity ranges between 0–2 times the molecular one, the corresponding contours in Fig. 4 (d) are clipped to highlight regions which have a high density of thermal subgrid-scale structures.

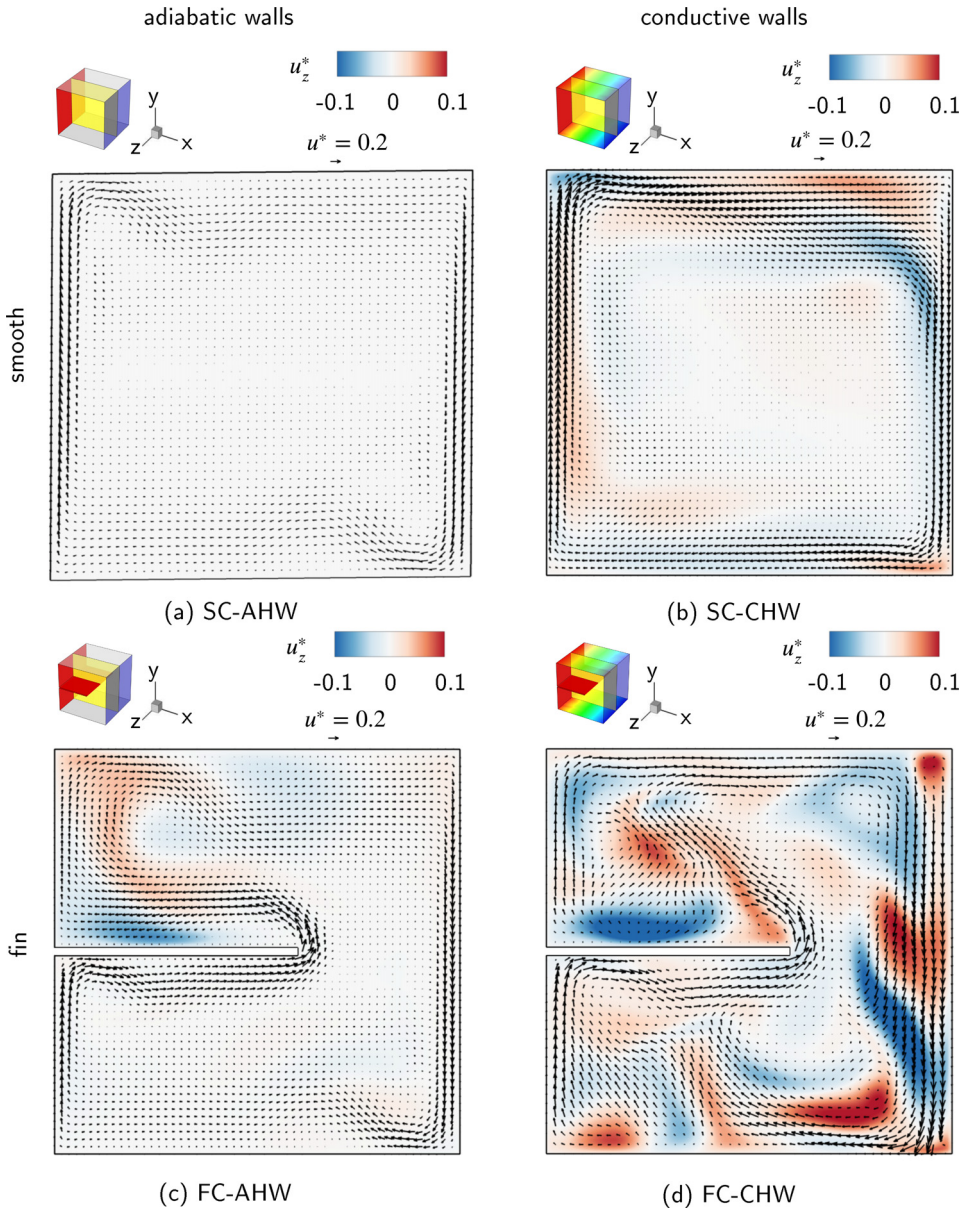

Fig. 5. Instantaneous 2D vector field of the in-plane velocity (i.e., in x-and y-direction) and contour map of out-of-plane velocity (i.e., the velocity in z-direction) for $Ra = 10^7$. Note that to improve the quality of presentation, results obtained on the original non-uniform mesh are mapped onto a uniform mesh. The velocities are scaled with the buoyancy velocity U_b for the corresponding Rayleigh number. Values outside the range $u_z^* = u_z/U_b \in [-0.1, 0.1]$ are clipped. The geometry and thermal boundary conditions are illustrated by sketches in the top-left corner of each subfigure.

5. Results and discussion

5.1. Velocity and temperature fields for adiabatic and conductive horizontal walls

5.1.1. Velocity field in smooth cavities

The instantaneous velocity field is depicted for $Ra = 10^7$ and $Ra = 10^9$ in Figs. 5 and 6, where the 2D vectors show the x- and y-components of the velocity, denoted as in-plane-velocity, and the contours depict the z-component of the velocity, denoted as out-of-plane velocity (Note the different scale for 6 (a) and (c), which were chosen to better highlight the structures). The velocities are normalized by the buoyancy velocity

$$U_b = \sqrt{gL\beta\Delta T}. \tag{13}$$

At $Ra = 10^7$, the in-plane velocity is highest in the proximity of the vertical isothermal walls in both the smooth cavities irrespective of adiabatic (SC-AHW, Fig. 5 (a)) or conductive horizontal walls (SC-CHW, Fig. 5 (b)). In the SC-AHW, the flow takes a turn away from the adiabatic horizontal wall at the leading edges (i.e., where the flow impinges onto a wall after a corner). (The cause for the turn is the high resistance due to the no-slip boundary in combination with a stable stratification due to the adiabatic walls.) This region of high curvature in the velocity was figuratively described as a hook-like structure by Puragliesi [59]. In contrast, in the SC-CHW, the flow remains attached to the conductive horizontal walls and the in-plane flow velocity remains high (Fig. 5 (b)). In the bulk regions, far away from the walls, the in-plane velocity is small in both the smooth cavities compared to the flow at the walls, Fig. 5 (a) and (b).

We observe that the normalized out-of-plane velocity, u_z^* (indicated by the contour) is negligible in the SC-AHW (Fig. 5 (a)). In contrast, in the SC-CHW, elongated regions of considerably high alternating positive or negative out-of-plane velocities occur next to

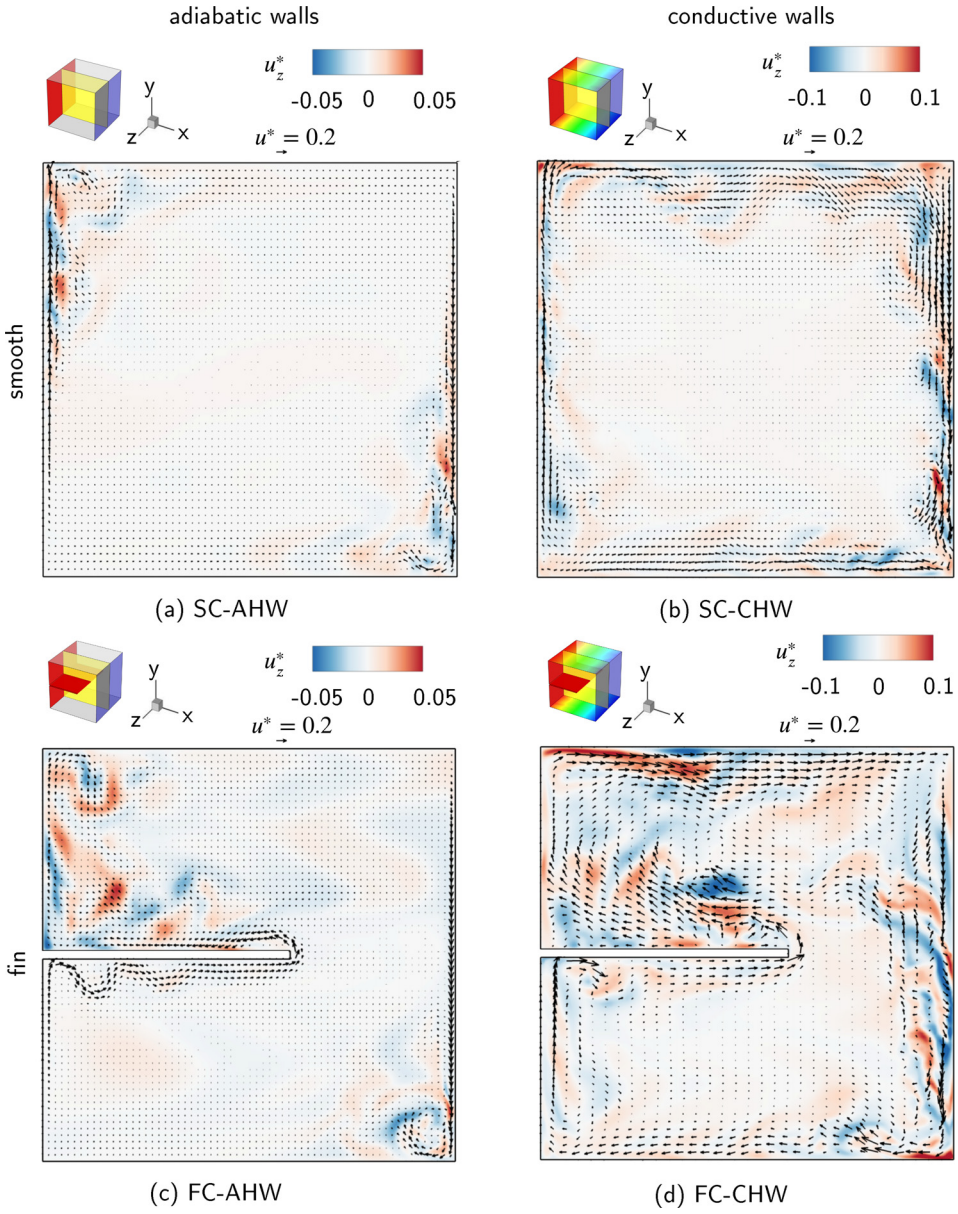

Fig. 6. Instantaneous 2D vector field of the in-plane velocity (i.e., in x-and y-direction) and contour map of out-of-plane velocity (i.e., the velocity in z-direction) for $Ra = 10^9$. Note that to improve the quality of presentation, results obtained on the original non-uniform mesh are mapped onto a uniform mesh of size. The velocities are scaled with the buoyancy velocity U_b for the corresponding Rayleigh number. Values outside the range $u_z^* \in [-0.1, 0.1]$ are clipped. The geometry and thermal boundary conditions are illustrated by sketches in the top-left corner of each subfigure.

each other in the vicinity of the horizontal walls (Fig. 5 (b)), implying the presence of 3D roll-like circulations.

At the higher Rayleigh number of $Ra = 10^9$, the in-plane and out-of-plane flow velocities are increased in the SC-AHW (Fig. 6 (a)) and in the SC-CHW (Fig. 6 (b)). The most striking change from lower to higher Rayleigh number appears in the out-of-plane velocity contours, as their direction is alternating at shorter spatial intervals with regions of high out-of-plane velocities restricted to the near-wall region. In the SC-AHW (Fig. 6 (a)), regions with strong three-dimensional flow features appear at the trailing edges of both the hot and cold vertical walls and the hook-like corner structure observed for the lower Rayleigh number is attenuated. However, in the SC-CHW (Fig. 6 (b)), these three-dimensional features are present throughout the regions near both vertical and horizontal walls. The flow instabilities induced by the conductive horizontal walls result in this behavior.

5.1.2. Velocity field in finned cavities

In this section, we discuss the addition of a fully conductive fin to the hot wall, with adiabatic horizontal walls (FC-AHW, Fig. 5 (c)) and with conductive horizontal walls (FC-CHW, Fig. 5 (d)). At $Ra = 10^7$ and for adiabatic horizontal walls (Fig. 5 (c)), the in-plane flow velocity (indicated by the velocity vectors) next to the non-finned vertical wall is similar to the one in the respective smooth cavity (Fig. 5 (a)). For conductive horizontal walls, the velocity is significantly increased and the high velocity region at the cold wall extends further into the bulk. In both the finned cavities, the flow velocity is highest close to the fin's edge (approximately $U/U_b = 0.3$). After the flow turns around the fin edge, it forms a smooth S-shape for the FC-AHW (Fig. 5 (c)), while it separates from the fin edge and ascends diagonally to the top for the FC-CHW (Fig. 5 (d)) (note that this is an instantaneous representation and especially the flow above the fin for the FC-CHW is subject to frequent changes). Both the finned cavities show enhanced out-of-

plane flow velocities compared to their smooth counterparts. For the FC-AHW (Fig. 5 (c)), a pair of a high positive and high negative velocity occurs above the fin. In contrast to the corresponding cavity with smooth walls, regions with small out-of-plane velocities appear in the corners next to the cold wall, implying a far-reaching effect of the fin on the onset of 3D flow. In the FC-CHW (Fig. 5 (d)), the magnitude of the out-of-plane velocities increases and the affected regions spread over the entire domain. The maximum out-of-plane velocity in the FC-CHW is around five times higher than the one of the FC-AHW.

At the higher $Ra = 10^9$ (Fig. 6), the flow velocity increases both in the plane and out of the plane. For the FC-AHW (Fig. 6 (c)), the flow meanders below the fin, while after the fin edge it remains closely attached to the upper side of the fin. In the FC-CHW (Fig. 6 (d)), the flow still rises after the fin edge, however, the slope is flatter than for $Ra = 10^7$. Similar to the smooth cavities (Fig. 6 (a), (b)), the regions with high out-of-the-plane velocity alternate at shorter spatial intervals. Unlike the smooth cavities where the three-dimensional structures are confined to the near-wall region, they also appear above the fin. In the FC-CHW (Fig. 6 (d)), the fin leads to enhanced three-dimensional structures even at the smooth, cold wall compared to the SC-CHW (Fig. 6 (b)). Thermal plumes — induced by the combined effect of the fins and conductive horizontal walls similar to Rayleigh-Bénard convection — intensifies the overall velocity magnitude and leads to such a strong three-dimensional flow. To understand these thermal plumes and other driving mechanisms in the velocity field, we analyse the temperature in the following section.

5.1.3. Temperature field in smooth cavities

Fig. 7 depicts the instantaneous temperature contours at a z-plane, in (a)–(d) for $Ra = 10^7$ and in (e)–(h) for $Ra = 10^9$. We first focus on the smooth cases at $Ra = 10^7$. For the SC-AHW (Fig. 7 (a)), a strong stable stratification sets in with hot fluid at the top and cold fluid at the bottom, which is supported by the adiabatic horizontal walls. At the vertical walls, the thermal boundary layer starts very thin at the leading edges and grows downstream. The involved steep temperature incline (decline) causes the strong buoyancy force, from which the high local velocity at the vertical walls originates (Fig. 5 (a)). When impinging on the adiabatic horizontal walls, the hook-like corner structure, which was previously perceived in the velocity field, is reflected in the temperature distribution as well: The heated (cooled) fluid follows the turn away from the wall and distributes over the upper (lower) part of the cavity. The flow crosses the cavity without big temperature changes (since the horizontal walls are adiabatic) yielding the very thin boundary layer at the leading edges of the opposite vertical wall. For the SC-CHW (Fig. 7 (b)), the bulk region exhibits a well-mixed temperature field with temperatures around $\Theta = 0.5$. The boundary layer at the vertical walls appears to be thicker than the one for adiabatic horizontal walls. At the conductive horizontal walls, local unstable temperature gradients disrupt the stable stratification causing a local convective mixing, as is evident from the higher in-plane and out-of-plane velocities (Fig. 5 (b)). This mixing results in a nearly isothermal bulk region. On the other hand, the mixing impedes the growth of a viscous boundary layer at the horizontal walls. Thus, the flow does not turn hook-like at the leading edges of the horizontal wall, but stays attached to it and can maintain a high velocity (Fig. 5 (b)). In addition, the conductive horizontal walls precool (preheat) the flow, before it impinges at the vertical walls. Consequently, the thermal boundary layer at the vertical walls starts relatively thick.

For the higher Rayleigh number $Ra = 10^9$ (Fig. 7 (e)–(f)), the thickness of the boundary layers at the vertical walls is reduced. For the SC-AHW (Fig. 7 (a)), oscillations disrupt the thermal boundary layer at the trailing edges of the vertical walls. However, in the cavity with conductive horizontal walls, the thermal boundary layer is wavy throughout the length of the vertical walls. This difference is attributed to the local alternating positive and negative out-of-plane velocity (Fig. 6 (a) (b)) which only occurred at the trailing edges for adiabatic horizontal walls, but could be observed along the entire neighborhood of all walls for the SC-CHW (Fig. 6 (b)).

5.1.4. Temperature field in a finned cavities

For the cavities with a conductive fin attached to the hot wall at $Ra = 10^7$, a hot boundary layer forms around the fin as shown in Fig. 7 (c),(d). The fluid is heated when flowing along the hot wall and below the fin, which yields a high temperature difference to its surroundings, when it rises at the fin tip. The high buoyancy force induces locally a strong rising flow (Fig. 5 (c),(d)), which entrains cold fluid from the region between the fin and the cold wall. In the FC-AHW (Fig. 7 (c)), a stronger stratification establishes in the upper part than in the smooth cavity and forms an enlarged high-temperature region above the fin. In the FC-CHW (Fig. 7 (d)), the conductive top wall does not only destabilize the flow locally — as it was already the case for the SC-CHW — but together with the hot fin induces a Rayleigh-Bénard convection kind of flow. This causes plumes rising from the fin and generating the intense circulations observed in the velocity field (Fig. 5 (d)).

At $Ra = 10^9$, the effects caused by the fin increase: In the FC-AHW (Fig. 7 (g)), the stratification becomes stronger yielding an enlarged high-temperature enclosure above the fin. In the FC-CHW (Fig. 7 (h)), the RBC-like plumes become spatially more frequent, which further enhances the three-dimensional flow, as observed in Fig. 6(d), and thus the mixing of the entire temperature field.

5.2. Three-Dimensional flow features

Instantaneous isosurfaces of the second-invariant of the velocity-gradient tensor (Q-criterion) [60] are shown in Fig. 8 (a)–(d) for $Ra = 10^7$ at $Q = 0.2s^{-2}$. For this value of Q, no structures are visible for the SC-AHW (Fig. 8(a), please note, that for visualizations using a smaller Q value, vortices near the top of the hot and bottom of the right wall would appear.), whereas for the SC-CHW (Fig. 8(b)), vortices stretch along the conductive walls as well as the leading edges of the vertical walls (i.e, the upper right and lower left corners). The vortices are caused by the unstable layering of cold fluid above hot fluid. In the inner corner above the fin of the FC-AHW, broad hair-pin vortices form quite distinctly (Fig. 8 (c)). Hair-pin vortices emerge from role vortices in the shear layer; disturbances deform them into Λ-vortices, whose heads rise from the wall, while the legs stay attached, which shapes the typical hair-pin shape, we observe in the figure (in the underlying case the corner may benefit the formation of the vortices). Though the Q-criterion can only depict vortices, the typical hair-pin shape strongly indicates the early stages of a transition to turbulence [61]. The fin case with conductive walls is filled with vortices except for a small bulk region below the fin.

For $Ra = 10^9$ more dense and stronger vortices occur, thus for the sake of clarity, we show the isosurfaces for the higher Q-value of $Q = 2s^{-2}$ in Fig. 8 (e)–(h). For the SC-AHW (Fig. 8 (e)), small vortices stretch along the trailing edges of the vertical walls. These streamwise roll vortices typically appear in boundary layers of driven flows at low Reynolds numbers [62]. Here, the high buoyant forces acting in the boundary layers drive the flow and cause this instability. When the flow takes a turn in the corner, the vortices vanish abruptly and at the adiabatic horizontal walls no instabilities are detected. In the SC-CHW (Fig. 8 (f)), the vortices in the vertical boundary layer get transported from the trailing edges across the corner and are still present at the leading edges of the conductive horizontal walls, but disappear at their center. At

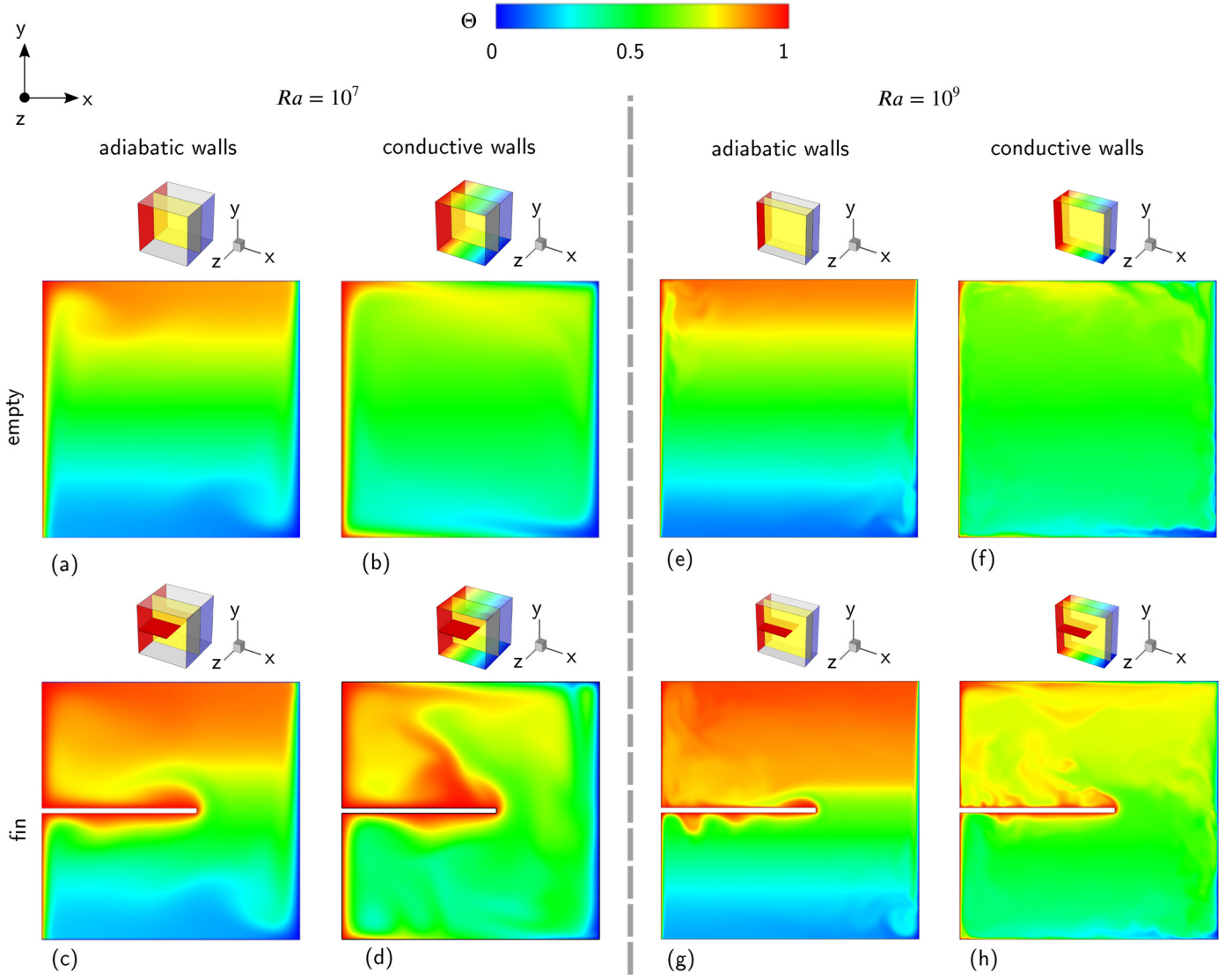

Fig. 7. Instantaneous temperature contours for (a)–(d) $Ra = 10^7$ and (e)–(h) $Ra = 10^9$. The geometry and thermal boundary conditions are illustrated by sketches in the top-left corner of each subfigure.

the trailing edges the local unstable stratification introduces vortices again, which trigger in the vertical boundary layer other vortices further upstream than for adiabatic horizontal walls. For the FC-AHW (Fig. 8 (g)), some eddies occur in the wall neighborhood above the fin. The structures at the upper part of the hot and lower part of the cold wall are damped compared to the smooth cavity. The FC-CHW (Fig. 8 (h)) experiences small vortices along all walls. Only below the fin, a stable stratification reduces the density of detected instabilities.

5.3. Boundary layer

The vortices, described in the previous section, disrupt the viscous boundary layer and reduce its thickness, and in presence of a temperature gradient, also the thermal boundary layer. The thermal boundary layer in turn directly influences the heat transfer (the thinner the thermal boundary layer, the higher the heat transfer). Therefore, we analyse the viscous and thermal boundary layer as a function of Rayleigh number. The viscous boundary layer thickness δ_u is defined by the distance from the wall at which the tangent of the kinetic energy profile at the wall and the horizontal line which crosses the maximum of kinetic energy k_{max} intersect [64], expressed as

$$\delta_u = k_{max}\left(\frac{\mathrm{d}\,k}{\mathrm{d}\,n}\right)^{-1}_{wall}.$$

The thermal boundary layer thickness δ_{th} is the distance from the wall at which the tangent of temperature profile at the wall and the tangent of the bulk temperature, i.e.,$\Theta = 0.5$, intersect, expressed as

$$\delta_{th} = (0.5 - \Theta_{wall})\left(\frac{\mathrm{d}\,\Theta}{\mathrm{d}\,n}\right)^{-1}_{wall}.$$

Since the fin influences the boundary layer at the hot wall, the boundary layer thickness was determined at the non-finned, cold wall ($x/L = 1.0$). The velocity and the temperature field were both time- and plane-averaged for the measurement of boundary layer thicknesses.

Fig. 9 depicts the viscous and thermal boundary layer thicknesses as a function of the Rayleigh number. We compare their slopes with the analytical Blasius relation [63] for laminar flow along a plate, which reads

$$\frac{\delta_u}{L} \propto Re^{-1/2} \propto Ra^{-1/4},$$

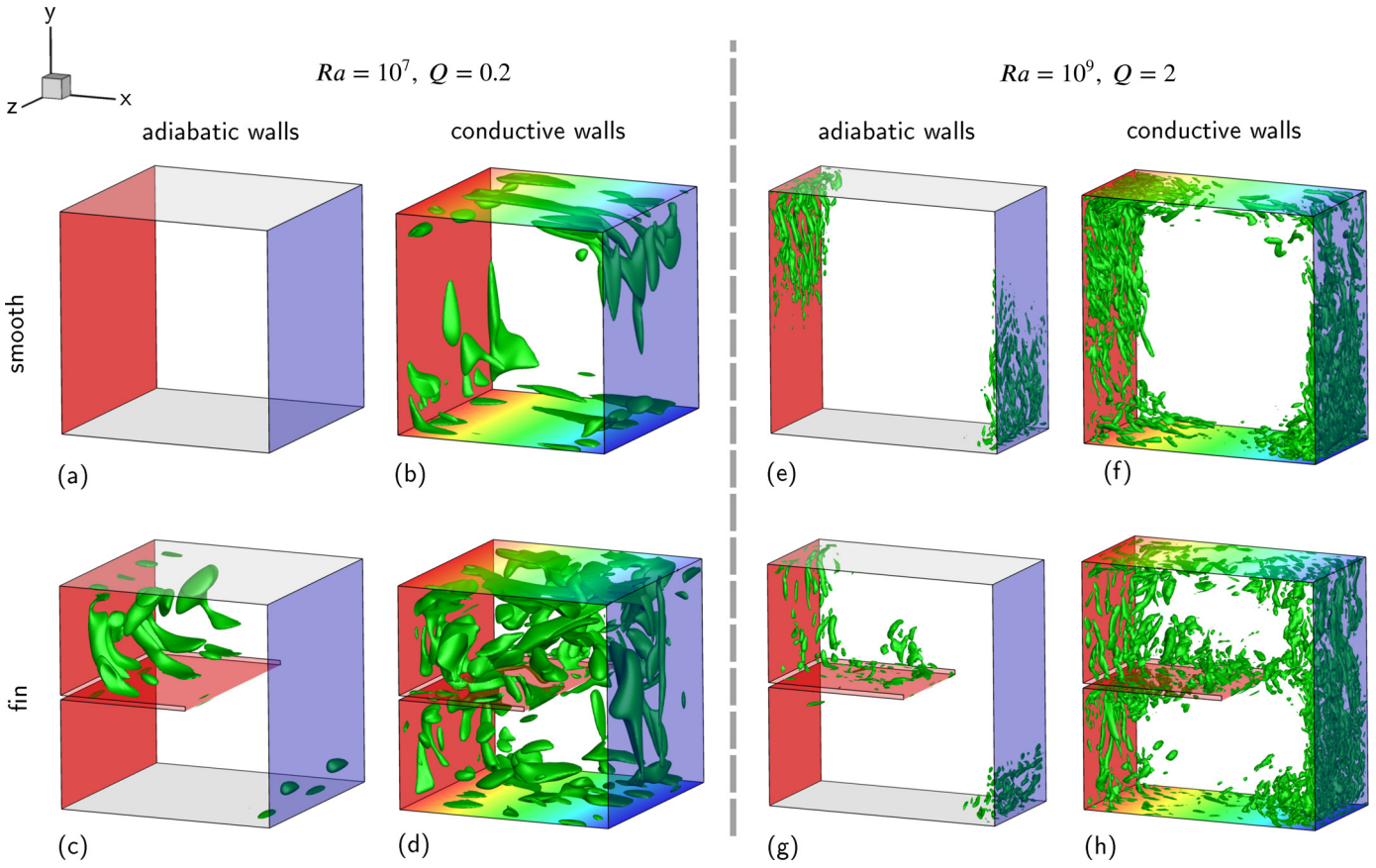

Fig. 8. Instantaneous Q-Criterion isosurfaces (a)–(d) at $Ra = 10^7$ for $Q = 0.2s^{-2}$ and (e)–(h) at $Ra = 10^9$ for $Q = 2s^{-2}$ (in green). The thermal boundary conditions are illustrated at the boundaries where the color corresponds to the legend in Fig. 7. (For interpretation of the references to colour in this figure legend, the reader is referred to the web version of this article.)

where the Reynolds number Re is based on the buoyancy velocity in Eqn. (13). For a laminar flow along a plate, the ratio between the viscous and thermal boundary layer is $\delta_{th} = \delta_u/\sqrt{Pr}$ for $Pr < 1$ [65]. For a constant Prandtl number, as in our case, this proportionality relation reduces to $\delta_{th} \propto \delta_u \propto Ra^{-1/4}$.

For all cases, the slope of the viscous boundary layer thickness closely follows the analytical approximation despite the turns the flow takes and the onset of 3D instabilities for higher Rayleigh numbers. The viscous boundary layer for the conductive cases is marginally thicker for both the cavities with conductive horizontal walls (i.e., SC-CHW and FC-CHW), which can be explained by the combination of two phenomena related to the conductive horizontal walls. First, the precooling (preheating) at the conductive horizontal walls reduces the temperature difference between the flow impinging at the leading edges of the vertical walls and the wall temperature, thus reducing the acting buoyancy force. Second, the 3D instabilities at the conductive horizontal walls disrupt the viscous boundary layer, reducing the shear resistance at the conductive horizontal walls compared to adiabatic horizontal walls (e.g., in the smooth cavities, the viscous boundary layer thickness is 0.047 at the conductive horizontal walls and 0.076 at the adiabatic horizontal walls). The thinner viscous boundary layers at the conductive horizontal walls permits the flow to take a smooth turn around the corners — instead of the hook-like flow for adiabatic walls (Fig. 5 (a)). This smaller resistance enables a stronger LSC (Fig. 5 (b)) and eventually allows high velocities not only in the direct neighborhood to the vertical walls, but a bit further away (Fig. 5 (b) and Fig. 6 (b)).

The thermal boundary layer thickness exceeds the viscous boundary layer for all considered cases — which is expected, since $Pr = 0.71$. The thermal boundary layer for the conductive cases is thicker than the one for the adiabatic cases, since the fluid is precooled along the conductive horizontal walls. The thermal boundary layer slopes deviate from the analytical expression. For a basic comparison of slopes, the data fit with $\delta_{th} \propto Ra^{\gamma}$ is denoted next to the thermal boundary layer line. The SC-AHW's thermal boundary layer slope of $\gamma = -0.272$ is close to the slope of the Blasius relation (Fig. 9 (a)).

For the conductive cases, the fluid gets precooled when flowing along the conductive top wall (refer to Fig. 7 (a), (b)), causing a thicker boundary layer at the cold wall than for adiabatic horizontal walls. On the other hand, the conductive horizontal walls trigger vortices spread along all walls at higher Rayleigh number (Fig. 8 (f)), which disturb the boundary layer. The slope of the SC-CHW (Fig. 9 (b)) is therefore marginally steeper ($\gamma = -0.284$) than the one for the SC-AHW ($\gamma = -0.272$).

The FC-AHW, depicted in Fig. 9 (c), has a similar thermal boundary layer thickness as the SC-AHW for low Rayleigh numbers, but with increasing Rayleigh numbers it reduces more rapidly (yielding an exponent of $\gamma = -0.306$). One could try to find the cause in the vortices again. However, the Q-criterion showed that the fin attached at the hot wall, dampens vortices at the cold wall, shown in Fig. 8 (g), compared to the smooth case. But if we look at the temperature field in Fig. 7 (g), we see that the strong stratification causes the thick layer of hot fluid, which forms between the conductive fin and the adiabatic top walls, to reach through to the cold wall, thereby causing a steep gradient in the temperature and a thin boundary layer. This effect increases with the Rayleigh number, thus giving the higher decay in thermal boundary layer thickness.

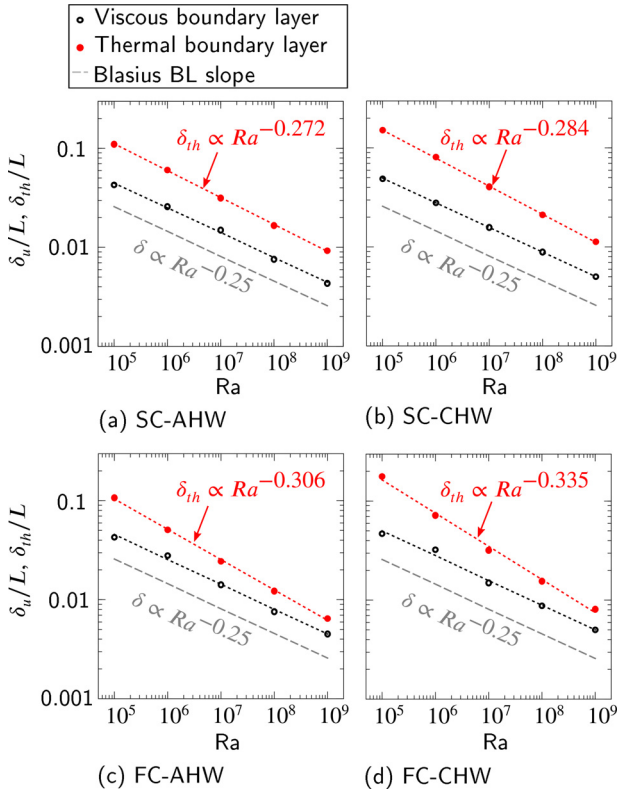

Fig. 9. Viscous and thermal boundary layer thicknesses at the cold wall for (a) SC-AHW, (b) SC-CHW, (c) FC-AHW and (d) FC-CHW. The gray dashed line plots the slope of the Blasius relation for a boundary layer at a plate [63], the dotted lines plot the power-law regressions for the boundary layer thicknesses.

The decline in thermal boundary layer thickness with Rayleigh number is the steepest for the FC-CHW with a power law coefficient of $\gamma = -0.334$ (Fig. 9 (d)), presumably due to the 3D instabilities in the entire boundary layer (Fig. 8 (g)) and the thermal plumes rising from the conductive fin towards the top wall, which cause a well-mixed temperature field in the bulk (Fig. 7 (d)).

5.4. Heat transfer

While our previous explorations of the flow field, vortices and boundary layers indicate how conductive walls and fins may affect natural convection in SHCs, our eventual aim is to enhance the heat transfer. The heat transfer is quantified by the dimensionless heat flux, i.e., the Nusselt number, defined as

$$Nu = \frac{hL}{k} = -\frac{\partial \Theta}{\partial n}\bigg|_w , \tag{14}$$

where h is the heat coefficient, L the characteristic length, k the conductivity, n denotes the direction normal to the surface and w the wall location.

The long-term time-averaged and spatially-averaged Nusselt number at the cold wall as a function of the Rayleigh number is shown in Fig. 10 (in (a) for the smooth and in (b) for the finned cavities). In both geometries, the heat transfer for adiabatic horizontal walls exceeds the one for conductive walls, since the latter precool (preheat) the fluid before it reaches the cold (hot) vertical wall. Note, that the Nusselt number at the cold wall does not include the total heat transfer of the cavity, as the conductive walls additionally transfer heat and the adiabatic walls do not. One could consider to include this additional heat transfer. However, as in technical applications often only the heat leaving via the cool side is decisive for the overall cooling of the system, we focus solely on the heat transfer across the vertical walls (an overview for the other walls is given in Appendix A). While the finned cases exhibit a marginally smaller Nusselt number for $Ra = 10^4$, their effectiveness to enhance heat transfer proves at high Rayleigh number, where the heat transfer is increased.

Table 4
Mean Nusselt Number magnitude at the Cold Wall at different Rayleigh numbers for all presented cases.

Ra	Nu_{cold}			
	SC-AHW	SC-CHW	FC-AHW	FC-CHW
10^4	2.3	1.7	2.1	1.5
10^5	4.6	3.3	4.9	3.3
10^6	9.0	6.6	9.9	6.7
10^7	16.7	12.7	19.0	15.0
10^8	30.4	24.1	35.1	28.8
10^9	54.8	45.1	64.5	54.7

The data for the smooth cavity are in excellent agreement with the reference data by Le Quéré and Behnia [13] and Sebilleau et al. [21]. The short-dashed lines denote the power law regressions, whose slopes, including the corresponding 95% confidence interval, are noted next to them. All slopes lie within the limits of laminar (0.25) and fully turbulent (0.33) scaling for RBC as derived analytically by Grossman and Lohse [17]. While the RBC setup is entirely different from the SHC studied here, multiple authors reported that the Rayleigh-Nusselt scaling for the SHC lies within these limits at sufficient high Rayleigh numbers [16,21], at which the convection dominates the heat transfer and the conductive part of transport is confined to the thin boundary layers. The perceived higher slope for conductive compared to adiabatic cases cannot be confirmed as the confidence interval is too large. This is due to the high standard deviation of the regression, which may indicate that the slopes change in the considered transition regime. The slope of the FC-CHW is higher than the ones for both the smooth cases (i.e., SC-AHW,SC-CHW) proving the enhancement of mixing in the transition regime by combining fins and conductive walls. Conductive walls reduce the integral Nusselt number at the cold wall by $\approx 30\%$ for lower Rayleigh numbers, at $Ra = 10^9$ this reduction lessens to $\approx 15\%$. The attachment of a fin reduces the heat transfer at $Ra = 10^4$, but increases it for higher Rayleigh up to $\approx 21\%$ for the FC-CHW at $Ra = 10^9$($\approx 18\%$ for the FC-AHW). In relation to the hot wall surface being increased by factor 2.2, this seemingly is not an efficient way to improve heat transfer. However, the crucial point is not the added wall length, but the fact that —using the same amount of space — heat transfer is enhanced significantly.

Since 3D simulations are quite expensive, multiple studies restrict themselves to 2D simulations, which cannot predict any 3D instabilities, not to mention turbulence [42–44]. Yu et al. [16] stated "that turbulence is not essential for the classical power law scaling of Nu" and obtained a scaling of $Nu \sim Ra^{0.31}$ for $Ra = 10^3$–10^7 using 2D simulations. To investigate any deviations the suppression of 3D instabilities brings, all simulations were repeated in 2D. For the smooth cavities, most Nusselt numbers from the 2D simulations match the 3D simulation results as shown in Fig. 10, with the exception of $Ra = 10^9$, for which the 2D simulations marginally underpredict the actual Nusselt value. For the finned cavities, 2D simulations underpredict the heat transfer from $Ra = 10^7$ upwards. While the deviations are marginal for adiabatic horizontal walls, they go up to 13% for conductive horizontal walls (Table 5) and are expected to rise with higher Rayleigh numbers. To determine the origins of these deviations, we analyze the local heat transfer in the next section.

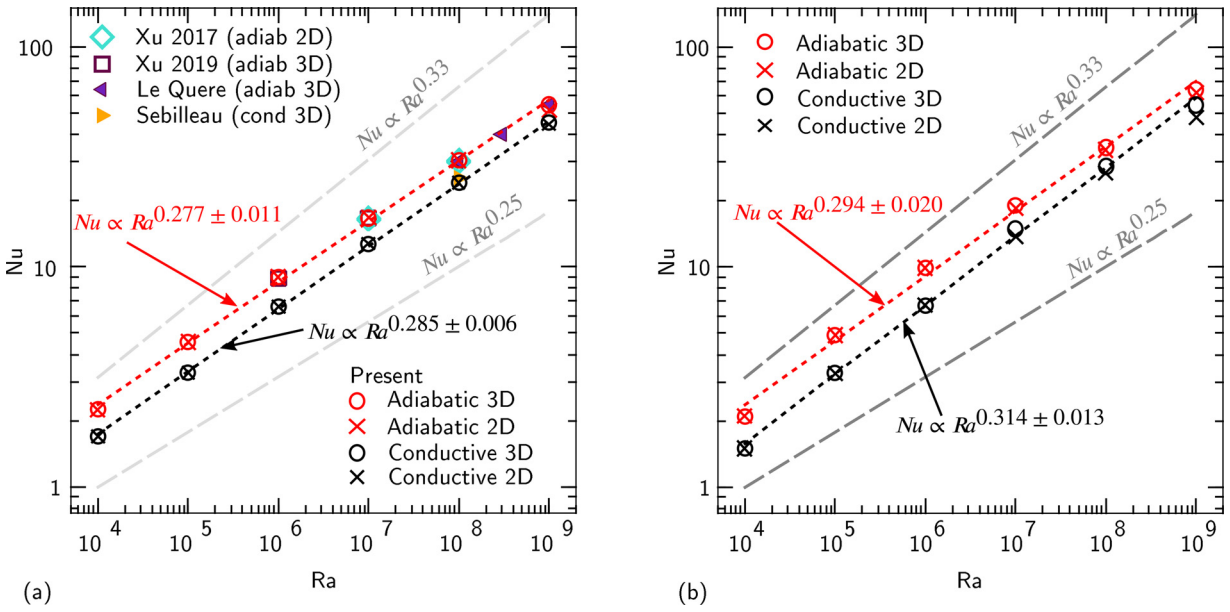

Fig. 10. Nusselt-Rayleigh relation at the cold wall for (a) the smooth cavity and (b) the finned cavity for 2D and 3D simulations. The dotted lines denote power law regressions, whose proportional relationship is given next to it with a 95% confidence interval for the slope. The dashed grey lines denote the laminar (power law exponent 0.25) and turbulent (power law exponent 0.33) limiting cases. The smooth cases are compared with data by Xu et al. [66,67], Le Quéré and Behnia [13] for adiabatic horizontal walls and Sebilleau et al. [21] for conductive horizontal walls. The Nusselt number values of the present simulations are listed in Table 4.

Table 5
Underprediction of the fin cases by 2D simulations.

Rayleigh number	Adiabatic fin case	Conductive fin case
$Ra = 10^7$	2.8%	8.7%
$Ra = 10^8$	2.8%	6.9%
$Ra = 10^9$	4.2%	13.0%

5.5. Local heat transfer

Though 3D instabilities spread over most wall regions in the SC-CHW at $Ra = 10^9$ (Fig. 8), it is surprising that the 2D-3D-deviation in the mean Nusselt number is small (Fig. 10). To provide more detailed insights into this behavior, we look at the local heat transfer predicted by the 2D and 3D simulations at $Ra = 10^9$. Fig. 11 displays the instantaneous local Nusselt number contours for the outer walls surrounded by line plots of the local Nusselt number along the corresponding wall, in which the local Nusselt number is depicted for

- the 2D simulations time-averaged,
- the 3D simulation time-averaged,
- and the 3D simulation instantaneous.

The values are extracted along a single line. In addition, the

- root-mean-square values of the 3D simulation instantaneous

is depicted (also along a single line and sampled over a long time). Both smooth cases show a symmetric time-averaged heat transfer. For the SC-AHW in Fig. 11 (a), the local Nusselt number starts at the leading edges of the hot wall with $Nu \approx 200$ and decreases first at a high and later at a lower rate further downstream. The instantaneous Nusselt number matches the averaged one, besides marginal oscillations in the second half of the walls, where the Nusselt contours show streamwise aligned streaks, which originate from the streamwise roll vortices, discussed in Section 5.2. Their influence sum up to the marginal 4.2% deviation between 2D and 3D simulations, listed in Table 5. Accordingly, the root-mean-square values of the Nusselt number are close to zero. For the SC-CHW (Fig. 11 (b)), the time-averaged Nusselt number is zero in the corners, then shows a steep peak of $Nu = 80$ at the leading edges and decays slowly when streaming along the vertical wall. The root-mean-square values illustrate the enhanced fluctuations compared to the SC-AHW. At the conductive horizontal top (bottom) wall the fluid is first heated (cooled) marginally, before the change in wall temperature switches the heat transfer to cooling (heating). The 2D simulation shows only modest deviations at the vertical walls, but a significant underprediction at the horizontal walls. In regions of 2D-3D-deviations, the instantaneous heat flux fluctuates indicating an influence of turbulent structures. Accordingly, the root-mean-square Nusselt number values are high at the leading edge, low in the center and then increase again. These oscillations are particularly accentuated in the Nusselt number contours, where streaks and a dendritic pattern can be observed. The latter indicates a breakdown of the initial roll vortices. For the SC-CHW, the vortices mainly enhance the precooling (preheating) at the top (bottom). The influence of the vortices on the vertical walls is small, which explains the good match between the 2D and 3D simulations for the mean Nusselt number at the cold wall of the SC-CHW in Fig. 10.

For the fin cases, we first focus on the Nusselt number at the outer walls, and discuss the fin itself in a later paragraph. For the FC-AHW (Fig. 11 (c)), the heat transfer is qualitatively similar to the one of the SC-AHW. It only deviates at the attachment point of the fin, where the Nusselt number is zero and downstream the fin the heat transfer over the hot wall is hardly perceptible. As in the SC-AHW, the root-mean-square values are also negligible here. When combining conductive horizontal walls and the fin (Fig. 11 (d)), both the local heat transfer and the 2D-3D-deviation are enhanced compared to the SC-CHW. This is especially the case at the top wall due to the thermal plumes, which rise from the fin towards the conductive top wall (Fig. 7). This gets reflected in enhanced root-mean-square values at the top wall.

The local Nusselt number at the fins itself is shown in detail in Fig. 12. At the lower side of the fins (Fig. 12 (a), (b)), the Nus-

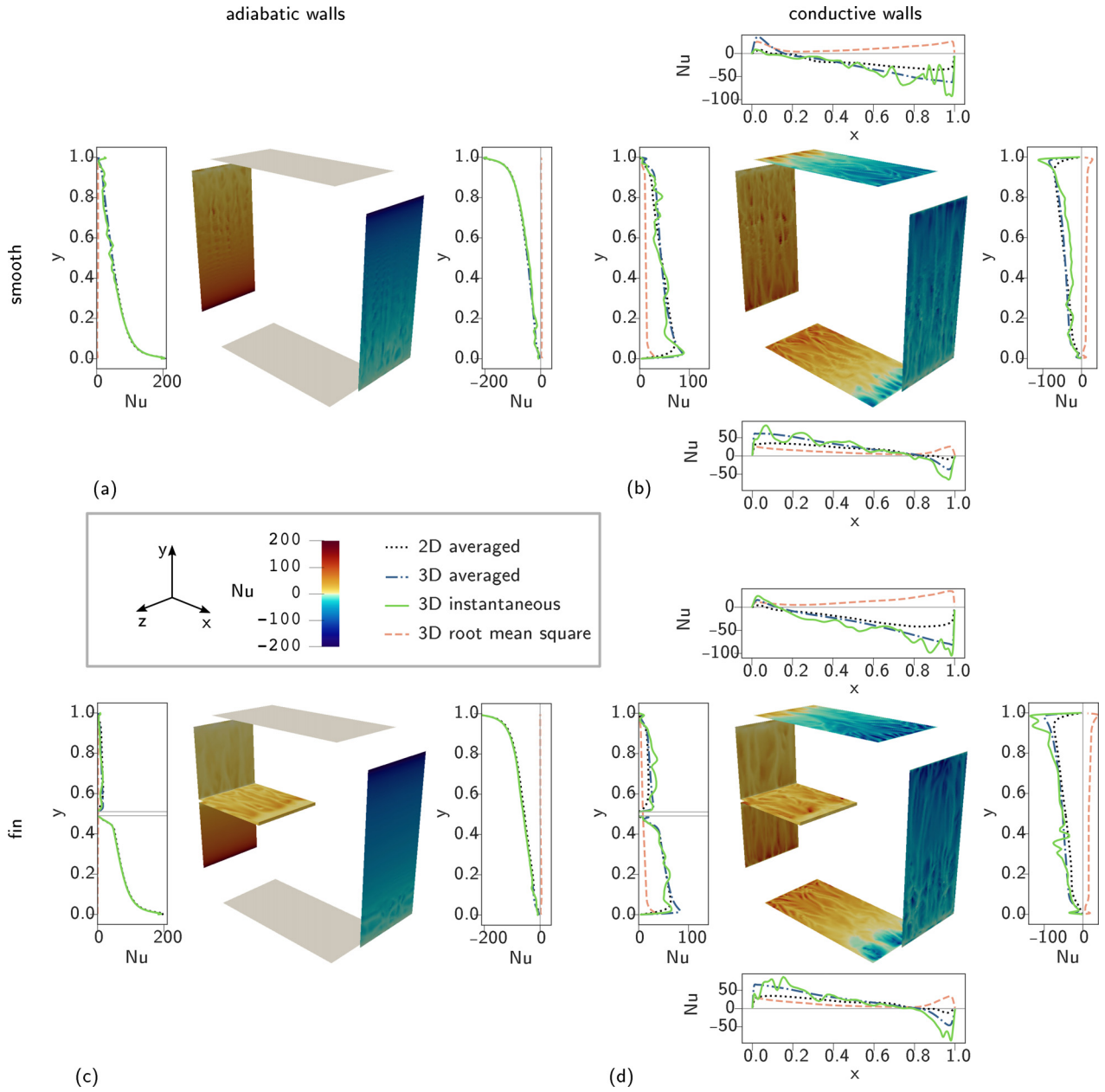

Fig. 11. Local Nusselt number for $Ra = 10^9$ for (a) the SC-AHW, (b) the SC-CHW, (c) the FC-AHW and (d) the FC-CHW. In the center local Nusselt number contours of all walls is shown, next to each (non-adiabatic) wall a line plot visualises for one line the time-averaged local Nusselt number from both the 2D and 3D simulations as well as an instantaneous local Nusselt number from the 3D simulation.

selt number shows several peaks coinciding with the minima of the thermal boundary layer below the fin (refer to Fig. 7 (g), (h)); the 2D simulation captures them qualitatively, but shifted. The 3D instantaneous line follows the 3D time-averaged line closely, indicating that the 2D-3D-deviation below the fin is not due to instabilities, but a change in the mean velocity field. This is supported by negligible root-mean-square values in most sections. High root-mean-square values occur only at the leading edge of the fin for the FC-CHW. At the upper side of the fins, the dimensionless heat flux drops when moving away from the fin tip — due to a small separation bubble, also visible from the velocity field in Fig. 6 — before rising to moderate values. The instantaneous 3D simulation results show fluctuations and root-mean-square values of the Nusselt number at the upper side, and the 2D simulation underpredicts the Nusselt number. Both the Nusselt number and its deviations are higher for the FC-CHW than for the FC-AHW. This is caused by the thermal plumes between the hot fin and the top wall, i.e. the Rayleigh-Bénard-convection behavior, which as well gives rise to the heat transfer enhancement previously described for the top wall. The lack of the third dimension clearly underpredicts the plumes — as the volume from which the plume rises cannot be replenished from the third direction — so heavily that the 2D simulation only predicts approximately 50% of the local heat transfer at the upper side of the fin. Thus, the reduction to two dimensions hinders the formation of vortices as well as thermal plumes and subsequently reduces the local heat transfer. This illustrates the necessity of performing full 3D simulations of natural convection in similar industrial setups even at moderate Rayleigh numbers.

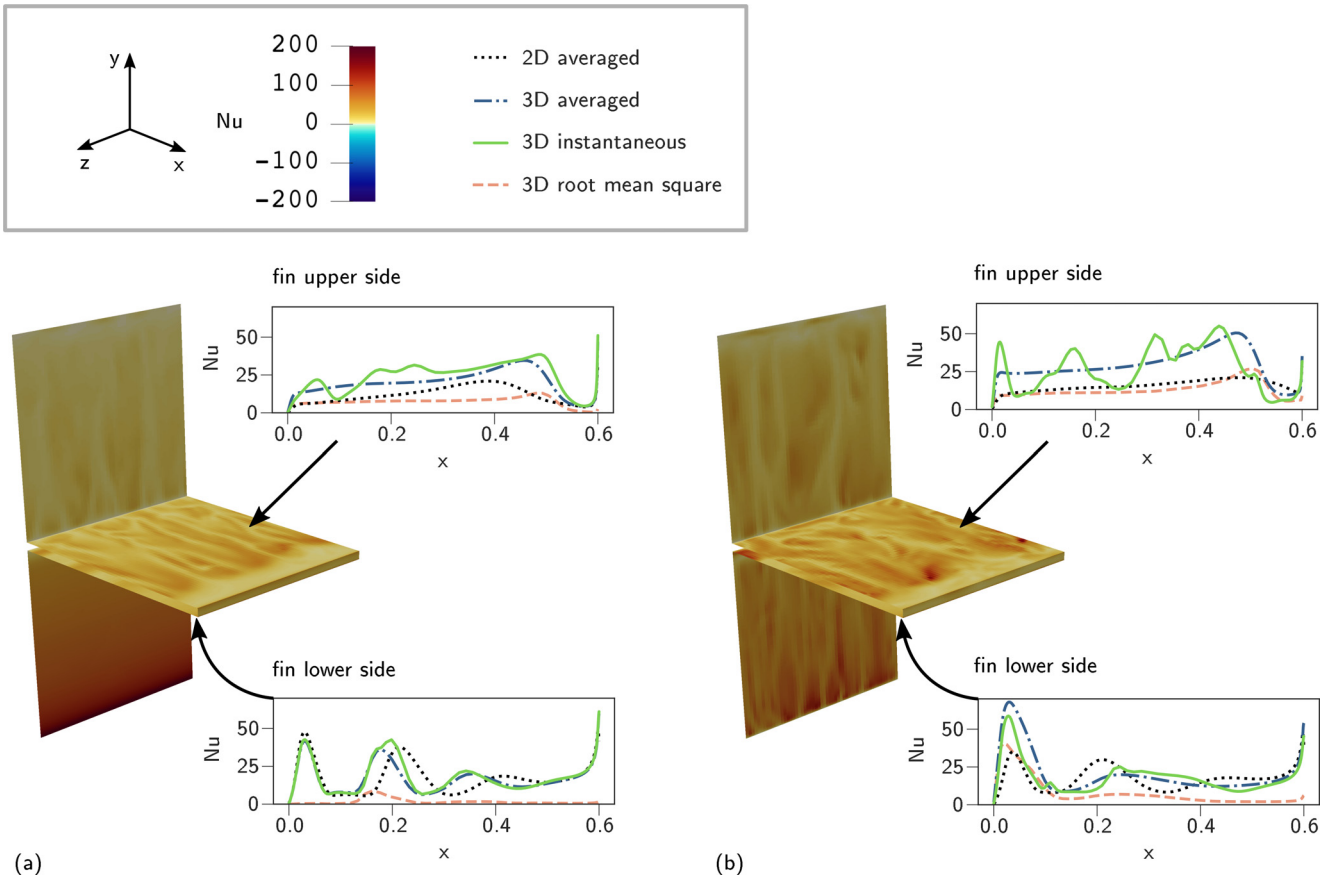

Fig. 12. The local Nusselt number plots for the upper and lower side of the fin (a) for adiabatic horizontal walls and (b) for conductive horizontal walls.

6. Conclusion

We studied the effect of conductive horizontal walls or a conductive fin attached to the hot wall on the heat transfer in a Side Heated Cavity using numerical simulations. We evaluated the flow for Rayleigh numbers between $Ra = 10^4$ and $Ra = 10^9$. We compared 2D and 3D simulations to assess the necessity of using 3D simulations.

The conductive horizontal walls introduce an unstable stratification at the top and bottom walls, thus triggering 3D instabilities, which disrupt the horizontal boundary layers and enhance the mixing of the fluid. The precooling/preheating along the conductive walls increases the thermal boundary layer thickness at the vertical walls, which entails a reduction in Nusselt number at these walls compared to the case for adiabatic horizontal walls. With increase in Rayleigh number this reduction lessens.

For both adiabatic and conductive horizontal walls, the addition of a fin at the hot wall gives an heat transfer enhancement compared to the non-finned cavities, which increases with Rayleigh and is $18 - 21\%$ at $Ra = 10^9$. 3D instabilities occur above the fin. For the adiabatic horizontal walls, however, the 3D instabilities at the cold wall are dampened compared to the smooth case and a large hot region forms between the fin and the adiabatic horizontal wall. The direct contact of this hot fluid region to the cold wall, gives an enhanced Nusselt number compared to the smooth cavity. For conductive horizontal walls, a Rayleigh-Bénard convection kind of flow sets in between the hot fin and the top wall. This significantly triggers 3D instabilities and yields a clearly enhanced slope in the Rayleigh-Nusselt relation compared to the other studied cases. Whether this high slope subsists at higher Rayleigh numbers and eventually even the heat transfer gain due to the fin overcomes the heat transfer loss due to the conductive horizontal walls, would be interesting to investigate, but was outside the scope of this study.

While the 2D and 3D simulations match well for the SC-AHW even at high Rayleigh numbers, this was not the case for the other cases: At both the upper side of the fin and at the horizontal conductive walls, the 2D simulations underpredicted the heat transfer locally by values up to 50%. On one hand this may yield undesirable, unforeseen hot spots in industrial applications potentially causing material damages, on the other it leads even to a total heat flux underprediction of 13% in the case of the FC-CHW. This emphasizes the need of resolving the flow also in the quasi-homogeneous third direction.

Declaration of Competing Interest

The authors declare that they have no known competing financial interests or personal relationships that could have appeared to influence the work reported in this paper.

CRediT authorship contribution statement

J. Elin Vesper: Conceptualization, Data curation, Formal analysis, Investigation, Software, Visualization, Writing – original draft. **Sebastian C. Tietjen:** Data curation, Formal analysis, Investigation, Methodology, Validation, Visualization, Writing – original draft. **Manu Chakkingal:** Conceptualization, Data curation, Formal analysis, Investigation, Methodology, Supervision, Validation, Visualization, Writing – original draft. **Saša Kenjereš:** Project administration, Resources, Funding acquisition, Visualization, Supervision, Writing – review & editing.

Acknowledgement

This work was carried out on the Dutch national e-infrastructure with the support of SURF Cooperative.

Appendix A. Mean Nusselt Number at All Walls for $Ra = 10^7$

Table A.1 states the time-averaged integral Nusselt number for all walls for $Ra = 10^7$. While the smooth cases give a symmetric heat balance, the conductive fin introduces additional heat, but diminishes the heat transfer at the vertical hot wall.

Table A1
Mean Nusselt Number at different walls for $Ra = 10^9$ for all presented cases.

	SC-AHW	SC-CHW	FC-AHW	FC-CHW
cold wall	-54.85	−45.25	−64.62	−55.08
hot wall without fin	54.85	45.25	41.98	35.43
fin	-	-	22.72	29.87
bottom	0	24.23	0	22.31
top	0	−24.25	0	−32.55

References

[1] D. Naylor, B.Y. Lai, Experimental study of natural convection in a window with a between-panes venetian blind, Exp. Heat Transfer 20 (1) (2007) 1–17, doi:10.1080/08916150600977358.
[2] O. Laguerre, D. Flick, Heat transfer by natural convection in domestic refrigerators, J Food Eng 62 (1) (2004) 79–88, doi:10.1016/S0260-8774(03)00173-0.
[3] S.M.S. Murshed, C.A.N. De Castro, A critical review of traditional and emerging techniques and fluids for electronics cooling, Renewable Sustainable Energy Rev. 78 (2017) 821–833.
[4] A. Sanghi, R.P.K. Ambrose, D. Maier, CFD Simulation of corn drying in a natural convection solar dryer, Drying Technol. 36 (7) (2018) 859–870.
[5] M. Simo-Tagne, M.C. Ndukwu, A. Zoulalian, L. Bennamoun, F. Kifani-Sahban, Y. Rogaume, Numerical analysis and validation of a natural convection mix–mode solar dryer for drying red chilli under variable conditions, Renew Energy 151 (2020) 659–673.
[6] K.B. Nasr, R. Chouikh, C. Kerkeni, A. Guizani, Numerical study of the natural convection in cavity heated from the lower corner and cooled from the ceiling, Appl Therm Eng 26 (7) (2006) 772–775.
[7] N. Williamson, S.W. Armfield, W. Lin, M.P. Kirkpatrick, Stability and Nusselt number scaling for inclined differentially heated cavity flow, Int J Heat Mass Transf 97 (2016) 787–793.
[8] S. Feng, M. Shi, H. Yan, S. Sun, F. Li, T.J. Lu, Natural convection in a cross-fin heat sink, Appl Therm Eng 132 (2018) 30–37.
[9] M.A. Sheremet, I. Pop, Natural convection combined with thermal radiation in a square cavity filled with a viscoelastic fluid, International Journal of Numerical Methods for Heat & Fluid Flow (2018).
[10] G.K. Batchelor, Heat transfer by free convection across a closed cavity between vertical boundaries at different temperatures, Q top Q. Appl. Math. 12 (3) (1954) 209–233.
[11] J.W. Elder, Turbulent free convection in a vertical slot, J. Fluid Mech (1) (1965) 99–111, doi:10.1017/S0022112065001258.
[12] S. Paolucci, D.R. Chenoweth, Transition to chaos in a differentially heated vertical cavity, J Fluid Mech 201 (1989) 379–410.
[13] P. Le Quéré, M. Behnia, From onset of unsteadiness to chaos in a differentially heated square cavity, J Fluid Mech 359 (1998) 81–107, doi:10.1017/S0022112097008458.
[14] F.X. Trias, A. Gorobets, M. Soria, A. Oliva, et al., Direct numerical simulation of a differentially heated cavity of aspect ratio 4 with Rayleigh numbers up to 10^{11} - Part II: heat transfer and flow dynamics, Int J Heat Mass Transf (2010), doi:10.1016/j.ijheatmasstransfer.2009.10.027.
[15] F.X. Trias, A. Gorobets, M. Soria, A. Oliva, et al., Direct numerical simulation of a differentially heated cavity of aspect ratio 4 with Rayleigh numbers up to 1011 - Part II: heat transfer and flow dynamics, Int J Heat Mass Transf (2010), doi:10.1016/j.ijheatmasstransfer.2009.10.027.
[16] H. Yu, N. Li, R.E. Ecke, Scaling in laminar natural convection in laterally heated cavities: is turbulence essential in the classical scaling of heat transfer? Physical Review E - Statistical, Nonlinear, and Soft Matter Physics 76 (2) (2007) 3–6, doi:10.1103/PhysRevE.76.026303.
[17] S. Grossmann, D. Lohse, Scaling in thermal convection: a unifying theory, J Fluid Mech 407 (2000) 27–56, doi:10.1017/S0022112099007545.
[18] A.M. Lankhorst, Laminar and Turbulent Natural Convection in Cavities: Numerical Modeling and Experimental Validation, Technische Universiteit Delft (The Netherlands), 1991 Ph.D. thesis.
[19] T. Fusegi, J.M. Hyun, K. Kuwahara, Three-dimensional natural convection in a cubical enclosure with walls of finite conductance, Int J Heat Mass Transf 36 (7) (1993) 1993–1997, doi:10.1016/s0017-9310(05)80185-1.
[20] R.A.W.M. Henkes, P. Le Quéré, Three-dimensional transition of natural-convection flows, J Fluid Mech 319 (1) (1996) 281–303, doi:10.1017/S0022112096007343.
[21] F. Sebilleau, R. Issa, S. Lardeau, S.P. Walker, et al., Direct numerical simulation of an air-filled differentially heated square cavity with Rayleigh numbers up to 10^{11}, Int J Heat Mass Transf (2018) 297–319, doi:10.1016/j.ijheatmasstransfer.2018.02.042.
[22] A. Sergent, P. Joubert, S. Xin, P. Le Quéré, et al., Resolving the stratification discrepancy of turbulent natural convection in differentially heated air-filled cavities part II: end walls effects using large eddy simulation, Int. J. Heat Fluid Flow 39 (2013) 15–27, doi:10.1016/j.ijheatfluidflow.2012.10.005.
[23] A. Liaqat, A.C. Baytas, Conjugate natural convection in a square enclosure containing volumetric sources, Int J Heat Mass Transf 44 (17) (2001) 3273–3280.
[24] M. Chakkingal, J. de Geus, S. Kenjereš, I. Ataei-Dadavi, M.J. Tummers, C.R. Kleijn, Assisting and opposing mixed convection with conjugate heat transfer in a differentially heated cavity filled with coarse-grained porous media, Int. Commun. Heat Mass Transfer 111 (2020) 104457.
[25] G.V. Kuznetsov, M.A. Sheremet, Numerical simulation of turbulent natural convection in a rectangular enclosure having finite thickness walls, Int J Heat Mass Transf 53 (1–3) (2010) 163–177.
[26] A. Nag, A. Sarkar, V.M.K. Sastri, Effect of thick horizontal partial partition attached to one of the active walls of a differentially heated square cavity, Numerical Heat Transfer; Part A: Applications 25 (5) (1994) 611–625, doi:10.1080/10407789408955969.
[27] A. Elatar, M.A. Teamah, M.A. Hassab, Numerical study of laminar natural convection inside square enclosure with single horizontal fin, Int. J. Therm. Sci. (2016), doi:10.1016/j.ijthermalsci.2015.08.003.
[28] T.L. Schulz, Westinghouse AP1000 advanced passive plant, Nucl. Eng. Des. 236 (14–16) (2006) 1547–1557, doi:10.1016/j.nucengdes.2006.03.049.
[29] N. Moummi, S. Youcef-Ali, A. Moummi, J.Y. Desmons, Energy analysis of a solar air collector with rows of fins, Renew Energy 29 (13) (2004) 2053–2064, doi:10.1016/j.renene.2003.11.006.
[30] S.Y. Kim, J.W. Paek, B.H. Kang, Flow and heat transfer correlations for porous fin in a plate-fin heat exchanger, J Heat Transfer 122 (3) (2000) 572–578, doi:10.1115/1.1287170.
[31] S. Humaira Tasnim, M.R. Collins, Numerical analysis of heat transfer in a square cavity with a baffle on the hot wall, Int. Commun. Heat Mass Transfer 31 (5) (2004) 639–650, doi:10.1016/S0735-1933(04)00051-X.
[32] F. Xu, J.C. Patterson, C. Lei, Transition to a periodic flow induced by a thin fin on the sidewall of a differentially heated cavity, Int J Heat Mass Transf (2009), doi:10.1016/j.ijheatmasstransfer.2008.06.030.
[33] J. Ma, B. Nie, F. Xu, Transient flows on an evenly heated wall with a fin, Int J Heat Mass Transf 118 (2018) 235–246, doi:10.1016/j.ijheatmasstransfer.2017.10.117.
[34] Y. Liu, S. Zhang, H. Huang, Q. Suo, Y. Bian, Y. Zhao, Enhancing the flow and heat transfer in a convective cavity using symmetrical and adiabatic twin fins, Int J Heat Mass Transf 142 (2019) 118447, doi:10.1016/j.ijheatmasstransfer.2019.118447.
[35] J. Ma, F. Xu, S.C. Saha, Flows and heat transfer of the transition to an unsteady state in a finned cavity for different Prandtl numbers, Int. Commun. Heat Mass Transfer 88 (October) (2017) 220–227, doi:10.1016/j.icheatmasstransfer.2017.09.012.
[36] Y. Liu, C. Lei, J.C. Patterson, Natural convection in a differentially heated cavity with two horizontal adiabatic fins on the sidewalls, Int J Heat Mass Transf 72 (2014) 23–36, doi:10.1016/j.ijheatmasstransfer.2013.12.083.
[37] R.A.W.M. Henkes, F.F. Van Der Vlugt, C.J. Hoogendoorn, Natural-convection flow in a square cavity calculated with low-Reynolds-number turbulence models, Int J Heat Mass Transf 34 (2) (1991) 377–388, doi:10.1016/0017-9310(91)90258-G.
[38] S.H. Peng, L. Davidson, Large eddy simulation for turbulent buoyant flow in a confined cavity, Int. J. Heat Fluid Flow (2001), doi:10.1016/S0142-727X(01)00095-9.
[39] Y.S. Tian, T.G. Karayiannis, Low turbulence natural convection in an air filled square cavity part II: the turbulence quantities, Int J Heat Mass Transf (2000), doi:10.1016/S0017-9310(99)00200-8.
[40] D.G. Barhaghi, L. Davidson, Natural convention boundary layer in a 5:1 cavity, Physics of Fluids 19 (12) (2007), doi:10.1063/1.2815746.
[41] A. Pilkington, B. Rosic, LES of Natural Convection in a Closed Cavity, in: Direct and Large-Eddy Simulation XI, Springer, 2019, pp. 307–313.
[42] K. Hanjalić, S. Kenjereš, F. Durst, Natural convection in partitioned two-dimensional enclosures at higher Rayleigh numbers, Int J Heat Mass Transf 39 (7) (1996) 1407–1427.
[43] S. Kenjereš, K. Hanjalić, Convective rolls and heat transfer in finite-length Rayleigh-Bénard convection: a two-dimensional numerical study, Physical Review E 62 (6) (2000) 7987.
[44] A.S. Gawas, D.V. Patil, Rayleigh-Bénard type natural convection heat transfer in two-dimensional geometries, Appl Therm Eng 153 (2019) 543–555.
[45] F. Toru, J.M. Hyun, K. Kunio, Transient three-dimensional natural convection in a differentially heated cubical enclosure, Int J Heat Mass Transf 34 (6) (1991) 1559–1564, doi:10.1016/0017-9310(91)90296-Q.

[46] M. Soria, F.X. Trias, C.D. Pérez-Segarra, A. Oliva, et al., Direct numerical simulation of a three-dimensional natural-convection flow in a differentially heated cavity of aspect ratio 4, Numerical Heat Transfer; Part A: Applications 45 (7) (2004) 649–673, doi:10.1080/10407780490277888.
[47] F.X. Trias, M. Soria, A. Oliva, C.D. Pérez-Segarra, et al., Direct numerical simulations of two- and three-dimensional turbulent natural convection flows in a differentially heated cavity of aspect ratio 4, J Fluid Mech 586 (2007) 259–293, doi:10.1017/S0022112007006908.
[48] I.V. Miroshnichenko, M.A. Sheremet, Turbulent natural convection heat transfer in rectangular enclosures using experimental and numerical approaches: areview, Renewable Sustainable Energy Rev. 82 (2018) 40–59.
[49] S. Xin, P.L. Quéré, Stability of two-dimensional (2D) natural convection flows in air-filled differentially heated cavities: 2D/3D disturbances, Fluid Dyn Res 44 (3) (2012) 031419, doi:10.1088/0169-5983/44/3/031419.
[50] O. Shishkina, R. Jam Stevens, S. Grossmann, D. Lohse, et al., Boundary layer structure in turbulent thermal convection and its consequences for the required numerical resolution, New J Phys 12 (17pp) (2010) 75022, doi:10.1088/1367-2630/12/7/075022.
[51] O. Shishkina, R.J.A.M. Stevens, S. Grossmann, D. Lohse, Boundary layer structure in turbulent thermal convection and its consequences for the required numerical resolution, New J Phys 12 (7) (2010) 075022, doi:10.1088/1367-2630/12/7/075022.
[52] R.I. Issa, Solution of the implicitly discretised fluid flow equations by operator-splitting, J Comput Phys 62 (1) (1986) 40–65.
[53] M. Chakkingal, R. Voigt, C.R. Kleijn, S. Kenjereš, Effect of double-diffusive convection with cross gradients on heat and mass transfer in a cubical enclosure with adiabatic cylindrical obstacles, Int. J. Heat Fluid Flow 83 (2020) 108574, doi:10.1016/j.ijheatfluidflow.2020.108574.
[54] P. Moin, K. Squires, W. Cabot, S. Lee, A dynamic subgrid-scale model for compressible turbulence and scalar transport, Physics of Fluids A: Fluid Dynamics 3 (11) (1991) 2746–2757.
[55] M. Wörner, Direkte Simulation turbulenter Rayleigh-Bénard-Konvektion in flüssigem Natrium, Kernforschungszentrum Karlsruhe, 1994 Ph.D. thesis.
[56] S. Kenjereš, K. Hanjalić, LES, T-RANS and hybrid simulations of thermal convection at high Ra numbers, Int. J. Heat Fluid Flow 27 (5) (2006) 800–810, doi:10.1016/j.ijheatfluidflow.2006.03.008.
[57] S. Kenjereš, Heat transfer enhancement induced by wall inclination in turbulent thermal convection, Physical Review E 92 (5) (2015) 053006.
[58] S.B. Pope, Ten questions concerning the Large Eddy Simulation of turbulent flows, New J Phys 6 (1) (2004) 35.
[59] R. Puragliesi, A. Dehbi, E. Leriche, A. Soldati, M.O. Deville, DNS Of buoyancy-driven flows and lagrangian particle tracking in a square cavity at high Rayleigh numbers, Int. J. Heat Fluid Flow 32 (5) (2011) 915–931.
[60] H. JCR, A. Wray, P. Moin, Eddies, stream, and convergence zones in turbulent flows, Center for turbulence research report CTR-S88 (1988) 193–208.
[61] Y. Motoori, S. Goto, Hairpin vortices in the largest scale of turbulent boundary layers, Int. J. Heat Fluid Flow 86 (2020) 108658.
[62] J. Kim, P. Moin, R. Moser, Turbulence statistics in fully developed channel flow at low Reynolds number, J Fluid Mech 177 (1987) 133–166, doi:10.1017/s0022112087000892.
[63] H. Blasius, Grenzschichten in Flüssigkeiten mit kleiner Reibung, BG Teubner, 1907.
[64] C.S. Ng, A. Ooi, D. Lohse, D. Chung, Vertical natural convection: application of the unifying theory of thermal convection, J Fluid Mech 764 (2015) 349–361, doi:10.1017/jfm.2014.712.
[65] H. Schlichting, K. Gersten, Boundary-layer theory, Springer, 2016.
[66] A. Xu, L. Shi, T.S. Zhao, Accelerated lattice boltzmann simulation using GPU and openACC with data management, Int J Heat Mass Transf 109 (2017) 577–588.
[67] A. Xu, L. Shi, H.-D. Xi, Lattice boltzmann simulations of three-dimensional thermal convective flows at high Rayleigh number, Int J Heat Mass Transf 140 (2019) 359–370.